Geotextiles and Geomembranes 54 (2026) 67–84

Contents lists available at ScienceDirect

Geotextiles and Geomembranes

journal homepage: www.elsevier.com/locate/geotexmem

Regular Paper

Effect of the driving process for construction of geotextile-encased columns on the deformation of soft foundation soils

H.P. Souza [a,*], G.L.S. Araújo [a], J.G. Zornberg [b], F.H.M. Portelinha [c]

[a] University of Brasília, Department of Civil and Environmental Engineering, Brasília, Brazil
[b] University of Texas at Austin, The University of Texas at Austin, Civil, Architectural and Environmental Engineering Department, USA
[c] Federal University of Sao Carlos, Civil Engineering Department, Washington Luis Rd., km 235, Sao Carlos, Sao Paulo, 13.565-905, Brazil

ARTICLE INFO

Keywords:
Geosynthetics
Transparent soil
Laponite RD®
Soft soil
GEC
PIV
Installation
Driving

ABSTRACT

The construction of geosynthetic encased columns for embankment support involving the tube driving technique may induce vertical and horizontal stresses throughout the soft soil foundation and neighboring columns, which is often not accounted for in design. Investigating this unknown effect is a difficult task for which the use of the transparent soil method is a promising tool when combined with Digital Image Correlation (DIC) techniques. This study investigates the effect of GEC column installation on the deformation of the soft foundation soil. The specific focus is on how the driving process affects the lateral and vertical deformations of the surrounding soft soil, as well as the interaction with neighboring columns. Different column configurations, spacing, and installation sequences were investigated. After evaluation and quantification of the deformation patterns, a methodology is proposed to study the extent of displacements caused by the tube's driving. Results showed that an increase in the spacing between columns reduced the influence of the tube's driving. Interestingly, adopting the alternating GEC installation may lead to higher lateral displacements than the sequential installation process. Increasing the number of GECs from three to four elements further reduced the displacements magnitude in the region adjacent to the first column installed.

1. Introduction

Granular soil columns constitute a ground improvement technique commonly used to enhance the bearing capacity of embankments founded on soft soils, accelerate their consolidation, and reduce embankment settlements. However, in very soft soils (e.g., with undrained shear strength S_u under 15 kPa), granular columns may experience excessive bulging and a reduced bearing capacity due to insufficient lateral confinement (FHWA, 1980; Kempfert and Gebreselassie, 2006; Hosseinpour et al., 2015). To address this issue, Geotextile Encased Columns (GECs) have often been adopted (Araújo et al., 2009; Almeida et al., 2014; Wu and Hong, 2014; Hong et al., 2016; Schnaid et al., 2017; Nagula et al., 2018; Alkhorshid et al., 2019; Orekanti and Dommaraju, 2019; Cengiz and Guler, 2020; Xu et al., 2021; Chen et al., 2022; Anita et al., 2023). The high stiffness geotextile casing involves the granular material and forms an encasement that is tensioned by radial stresses mobilized on the granular material when the GEC is loaded. This system works both as a drainage mechanism and a pile, effectively transferring the load to the underlying strata.

The GEC installation process may involve vibro-replacement techniques, which involve initially driving a closed-end steel vibrated casing into the soft foundation up to the resistant soil layer. Then, the casing is filled with granular material and the steel tube vibrates out of the ground while compacting the granular material. The driving process generates lateral displacements on the surrounding soft ground and propagates toward adjacent GECs. The effectiveness of the column installation process plays a significant role in the behavior of encased granular columns (Castro and Karstunen, 2010) and several field monitoring studies have been conducted to investigate the effect of the GEC's installation on soft soils in increasing horizontal stresses and pore water pressure (Watts et al., 2000; Kirsch, 2004; Castro, 2008; Araújo et al., 2009; Schnaid et al., 2017; Wang et al., 2023; Ouyang et al., 2024). Additionally, previous studies have conducted numerical simulations to evaluate the impact of the installation approach on the soil foundation surroundings (Nagula et al., 2018; Shehata et al., 2018; Geramian et al., 2022; Kelesoglu and Durmus, 2022). For instance,

* Corresponding author.
E-mail addresses: henrique.petisco@gmail.com (H.P. Souza), gregorio@unb.br (G.L.S. Araújo), zornberg@mail.utexas.edu (J.G. Zornberg), fportelinha@ufscar.br (F.H.M. Portelinha).

https://doi.org/10.1016/j.geotexmem.2025.09.006
Received 22 July 2025; Received in revised form 1 September 2025; Accepted 25 September 2025
Available online 11 October 2025

Castro and Karstunen (2010) modeled stone column installation to evaluate its impact using the cavity expansion method coupled with advanced soil models to quantify on soft soils. The results showed that the process resulted in excess pore pressures and increased horizontal stresses on the soil foundation after the end of the stone columns installation by vibro replacement.

Quantifying the effect of GEC installation in a full-scale project would involve a significant array of sensors and complex interpretations on field or laboratory tests, while numerical simulations may not capture the physical mechanisms of the materials under investigation. In this context, experimental techniques that allow visualization of the system would be very beneficial. Transparent soil techniques such as those adopted in recent geotechnical investigations (e.g. Cao et al., 2011; Ezzein and Bathurst, 2014; Peng and Zornberg, 2019; Chen et al., 2022; 2019a; Ads et al., 2020a; 2020b; Liu et al., 2020; Yuan et al., 2020; Zhang et al., 2019; Chen et al., 2021; Xu et al. 2021; Zhang et al., 2019; Ma et al., 2023; Wang et al., 2023; Yang et al., 2022) have the potential to provide insight into the impact of the GEC installation over soft foundation soils.

Synthetic magnesium lithium phyllosilicate, commercially known as Laponite RD®, is a transparent soft clay surrogate that has been adopted in geotechnical investigations (Beemer and Aubeny, 2012; Wallace and Rutherford, 2015; Beemer et al., 2016; Ads et al., 2020a; 2020b; Pierozan et al., 2021; Almikati et al., 2023). This material represents a transparent soil that exhibits geotechnical properties comparable to very soft natural firsts (Wallace and Rutherford, 2015) and has been employed to develop scaled physical models (Chini et al., 2015; Ads et al., 2019a; 2020b, 2021c; Zhang et al., 2019) with potential application of the Digital Image Correlation (DIC) technique to measure displacements and strains by tracking pixel movements in sequential images (Helm and Suleiman, 2012; Khatami et al., 2019; Li et al., 2019; Ren et al., 2022; Kim et al., 2022; Salehzadeh et al., 2022; Sharifi et al., 2022). Although several studies have evaluated the behavior of GECs, publications about the effects of their installation are lacking and the potential application of Laponite RD® on physical models in this case may contribute to fill this lack.

In this investigation, small-scale 1-g physical models using Laponite RD® as a transparent surrogate for soft soil were employed to evaluate the effect of closed-end driving tubes of GECs on lateral displacements and strains. The Digital Image Correlation (DIC) technique was used to infer the displacements on the transparent soil originating from the procedure. In this technique, the displacements of the pixel on sequential images are tracked and converted to displacements in metric values from a calibration factor obtained previously (Stanier et al., 2016). This study examines the installation effects on adjacent columns, comparing the influence of differently sequenced installation processes and spacing between columns. The paper also proposes an analytic approach to predict the extent of displacements caused by the driving process.

2. Transparent 1-g physical GEC models

2.1. Scale factors

The use of 1-g physical models requires that the selected material properties be properly scaled to match those of a prototype (real-scale problem). This scaling is typically achieved by applying the similitude criterion as outlined in Equation (1) (e.g., Hong et al., 2016):

$$\frac{I_p}{I_m} = S_f \tag{1}$$

where I_p is the prototype parameter value; I_m is the scaled model parameter; and S_f is the scale factor. In this investigation, the prototype was assumed to have a square grid layout (Hosseinpour et al., 2016), with GECs measuring 0.8 m in diameter (D) (a typical field value), spaced 2.0 m apart (S) and installed in a 10-m-thick soft foundation soil layer resting on a firm stratum. The undrained shear stress (S_u) and thickness of the soft soil layer (H); the unit weight (γ) and effective friction angle (ϕ') of the granular material; and the tensile strength (T_g) and secant stiffness ($J_{g,5\ \%}$) of the geotextile were also compatible with the similitude criteria. Table 1 summarizes the scale factors compatible with the similitude criteria to each parameter of the 1-g physical model developed in this study.

2.2. Materials used

In this study, a transparent soft foundation with an undrained shear strength (S_u) of 0.25 kPa was used to simulate soft soil with a S_u of 10 kPa, a very soft material that can be encountered in several embankment projects. To characterize the desired material properties, vane shear tests were performed on Laponite RD® solutions with concentrations of 4 %, 6 %, 8 % and 10 %, and kept consolidating for periods of three, seven and 14 days. Sodium Pyrophosphate Decahydrate (SPP) was added to samples with concentrations greater than 4 % to allow mix the Laponite RD® solution without phase separation as recommended by Beemer et al. (2016). Table 3 summarizes the undrained shear stress (S_u) results obtained for Laponite under different tests configurations.

Based on the results, the Laponite RD® sample with a 4 % mass concentration and seven-day set period achieved the target undrained shear strength of approximately 0.25 kPa, consistent with the 1/40 scale factor adopted in this study. Additionally, the selected set time and Laponite dosage exhibited sufficient transparency for accurate visualization in PIV analysis. After determining the soft soil surrogate material, geotechnical characterization tests were conducted, the results of which are summarized in Table 4. A comparison of these results with those obtained by Wallace and Rutherford (2015) under similar conditions confirmed that the values obtained herein are comparable.

Commercial fabric material was chosen to represent the geotextile under the similitude conditions imposed on the scaled model and used to manufacture the geosynthetic encasement. Wide-width tensile tests were performed to characterize its ultimate tensile strength and secant stiffness (ASTM D4595-17, 2023). The selected material exhibited an ultimate tensile strength of $T_g = 1.21$ kN/m and $T_g = 0.551$ kN/m, respectively, and secant stiffness values of $J_{g,5\ \%} = 7.73$ kN/m and $J_{g,5\ \%} = 2.15$ kN/m in the machine and cross-machine directions, respectively. Based on the obtained results, the encasement was used with radial mobilization in the cross-machine direction as it was more compatible with the radial stiffness and tensile strength of the prototype scale. Tensile tests were also performed to evaluate the seams needed to produce the encasement and the results indicated their full efficiency as the fabric break occurred only at the same maximum tensile strength of the fabric itself. However, the presence of the seam reduced the stiffness to 1.34 kN/m, while an ultimate tensile strength of 0.551 kN/m was maintained as depicted in Table 5. Considering the scale factors in Table 1, the selected encasement material simulated a geotextile with 880 kN/m of ultimate tensile strength and a secant stiffness of 2144 kN/m.

A uniformly graded SP fine sand with particle sizes ranging from 0.075 mm to 0.42 mm was used as the column granular material. Table 6 summarizes the parameters of the granular soil. The granular material

Table 1
Scale factors corresponding to relevant properties of the materials used in this study.

Element	Properties	Scale Factor	Prototype values
Soft Clay	S_u (kPa)	(1/N)	≤10.0
	H (m)	(1/N)	9–10
Granular Soil	γ (kN/m^3)	1	20.0
	ϕ'(°)	1	45.0
	D (m)	(1/N)	0.80
Geotextile Encasement	T_g (kN/m)	(1/N)^2	≥150 kN/m
	$J_{g,5\ \%}$ (kN/m)	(1/N)^2	≥2000 kN/m

Table 2
Characteristics of experimental models.

Model	Number of GECs	Model spacing	Prototype spacing (S)
M1S2	1	–	One single column
M2S1S	2	25.0 mm	1.0 m
M2S1.5	2	37.5 mm	1.5 m
M2S2	2	50.0 mm	2.0 m
M2S2.5	2	62.5 mm	2.5 m
M3S2A, M3S2S	3	50.0 mm	2.0 m
M4S2S	4	50.0 mm	2.0 m

Table 3
Results of S_u after vane shear tests on Laponite.

Material	Content (%)			
Laponite RD®	4	6	8	10
SPP	–	0.13	0.27	0.75
Set time	Undrained shear strength (S_u)			
3 days	0.175	0.370	0.583	0.800
7 days	0.262	0.450	0.750	0.950
14 days	0.333	0.570	0.770	0.970

Table 4
Laponite RD® parameters.

Property	Obtained	Wallace and Rutherford (2015)
Liquid Limit (W_L)	958 %	1150 %
Plastic Limit (W_P)	250 %	240 %
Plasticity Index (IP)	707 %	910 %
Hidraulic conductivity (k_s)	$1{,}25.10^{-7}$ – $1{,}06.10^{-6}$ cm/s	$3{,}00.10^{-7}$ – $1{,}60.10^{-6}$ cm/s
Specific Gravity (G_s)	2.53 (Provided by the manufacturer)	
Initial void ratio (e_0)	53.0	56.5
Compression index (C_c)	19.9	20.4

Table 5
Geotextile encasement tensile properties.

Property	J_g (kN/m)	T_g (kN/m)
Machine Direction (MD)	7.73	1.21
Cross-machine Direction (CMD)	2.15	0.55
Seam	1.34	0.55

Table 6
Sand parameters.

Property	Obtained
D_{60} (mm)	0.32
D_{30} (mm)	0.25
D_{10} (mm)	0.15
Uniformity Coefficient (C_u)	2.53
Coefficient of Curvature (C_c)	1.10
Soil Classification	SP
Maximum Void Ratio (e_{max})	0.962
Minimum Void Ratio (e_{min})	0.769
Specific Gravity (G_s)	2.71
Effective friction angle, $\phi'(^\circ)$	46°

was gradually added into the driving tube using a funnel positioned at its upper opening. The granular material was compacted by vibration, with the mass and volume of the material carefully controlled to achieve a target relative density greater than 80 %. The tube was removed in stages as the GEC was filled.

2.3. Laboratory tests

The experimental models were constructed at a 1/40 scale to simulate a full-scale prototype with corresponding dimensions. Transparent clay was placed in a plexiglass box measuring 350 mm × 500 mm x 200 mm, with the analysis section, which refers to the area where particle movement was observed during testing, positioned 150 mm from the front transparent wall to minimize boundary effects and maintain transparency in the analysis section. Fig. 1-a shows the 250 × 500 mm cross-section for a model build on this study observed the beginning of the installation of the last out-of-three GECs using a plexiglass tube. The GECs are regularly spaced and have their tips settled on a sand drain with 50 mm thickness. The observation cross-section had a 3 mm width and was seeded with randomly distributed particles usually applied to track the displacements on some transparent soil types in DIC analysis (Iskander, 2010; Ads et al., 2021; Ergin, 2021; Ren et al., 2023).

The GEC installation considered driving a 25.0 mm external diameter closed-tip tube with micro-vibration motors attached to its upper extremity into the transparent soil until it reached the firm stratum at the bottom of the box, with ratio of 10 mm/s. Subsequently, the geotextile encasement was placed inside the tube and then filled with the filling material. The driving tube was subsequently extracted from the soft foundation maintaining its vibration. The compaction aimed a relative density greater than 80 % which was controlled by the fill material mass used in the GEC and the column's final volume. The GEC's final volume was calculated after obtaining its average diameter on the images captured for DIC analysis at the end of installation, considering the corresponding scale. The relative density also considered the maximum and minimum void ratio for the fill material.

Fig. 1-b shows the support used to guide the tube inside the soft foundation soil during the driving and the camera located at the center in front of the plexiglass box and focused on the section analysis. The driving support had a mobile plate with a hole that allowed change the tube insertion position. Fig. 1-c shows the plexiglass tube, with vibration motors, inserted on the driving support hole and the soil foundation. In this case, the geotextile encasement is observed inside the tube with the sand funnel used to put the granular material within it.

A total of eight physical models were constructed and tested in this study. One configuration involved a single GEC installed using a driving tube, with observations and measurements of displacements of the transparent soil surrounding the GEC. The other physical models were constructed to investigate the effects of installing multiple GECs in soft foundation, considering two, three, and four columns. For models with two GECs, the effect of different horizontal spacings (S) between columns—1.0 m, 1.5 m, 2.0 m and 2.5 m at prototype scale—were assessed. In models involving three and four columns, a typical field spacing of 2.0 m between GECs at prototype scale was adopted (Alexiew et al., 2005; Almeida et al., 2019). These tests aimed at evaluating the effect of two different installation orders (involving three columns) and the efficiency of a higher number of GECs (four columns) in mitigating lateral stresses on surrounding GECs and neighboring structures. The models with three GECs considered two column installation sequences: (i) first driving the two external GECs followed by one in between; and (ii) sequentially installing the GECs. The model with four columns involved the sequential installation of all columns.

To facilitate the understanding of the configurations, the models were abbreviated with acronyms containing four to five characters describing their major characteristics. For example, in the acronym "M1S2," M denotes "Model," 1 refers to the quantity of columns, S denotes "Spacing" and 2 refers to the adopted spacing value in meters (m) at the prototype scale. For models with three or more GEC, a final fifth character was used to indicate its order of installation: "A" indicates the alternate installation (odd GECs first then even) and "S" the sequential installation (sequentially in row). Table 2 summarizes all the configurations and Fig. 2 shows the installation sequences.

Testing of the physical models included capturing sequential images

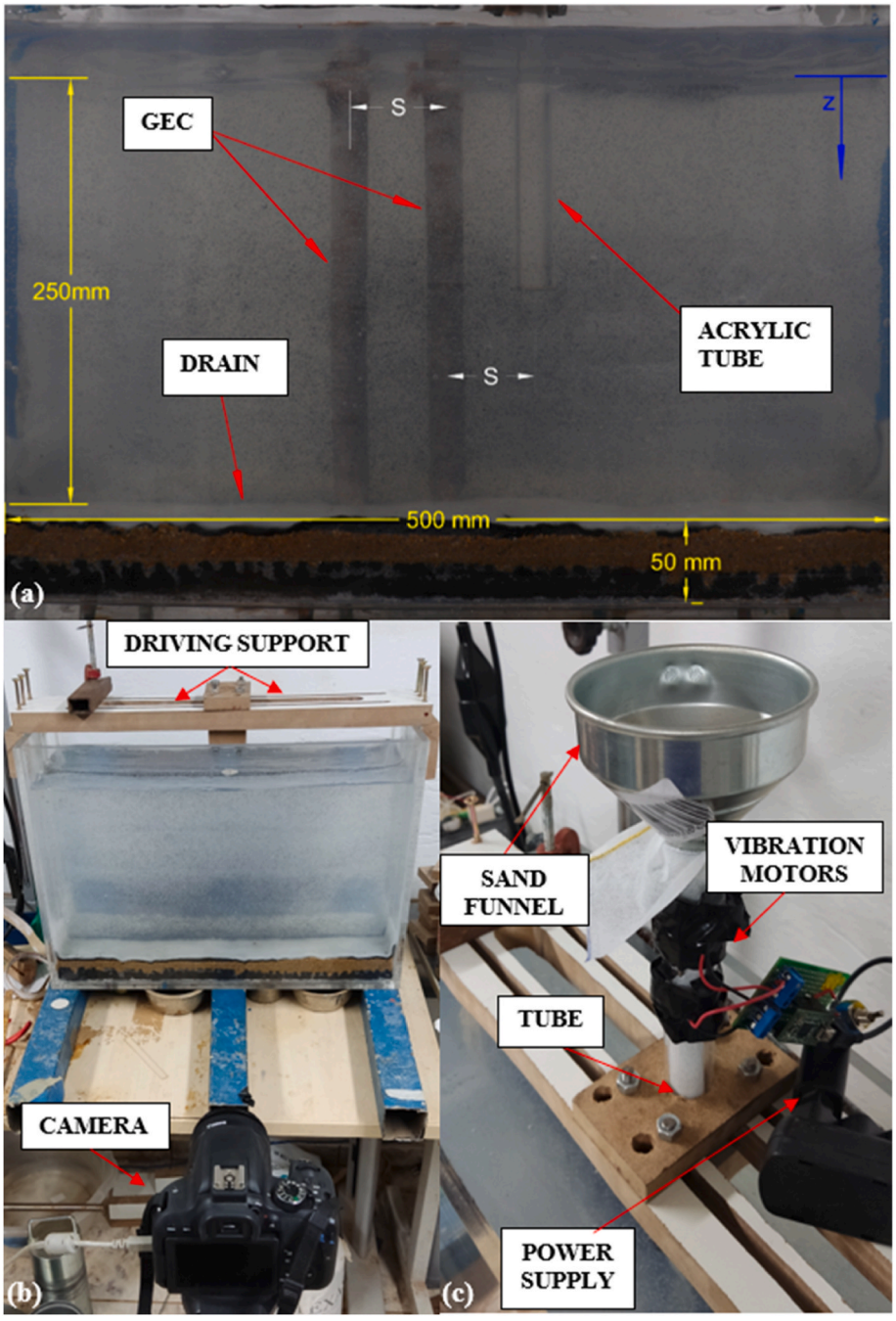

Fig. 1. Setup of transparent models: (a) plexiglass box geometry for model; (b) image acquisition system; and (c) tube driving system.

of the analysis section while the tube was driven into the transparent soil for subsequent DIC analysis. Images were taken at 1-s intervals using a camera set to a resolution of 2976 x 1987 pixels, with ISO 100, an aperture of f/6.3, and a shutter speed of 1/250. The software PIVLab (Thielicke and Stamhuis, 2014), an open-source tool developed in MATLAB, was used for PIV analysis. Before analyzing particle movements with PIVLab, the images were pre-processed using Contrast Limited Adaptive Histogram Equalization (CLAHE), used to improve the contrast on images, and intensity capping filters along with the software's auto-contrast feature.

3. Results

The results of the experimental testing program are divided into four sections, each one addressed to a respective number of GECs installed on a model. The analysis adopted the horizontal (u) and vertical (v) directions fields of the displacements within the soft foundation soil as main results as it allowed to observe patterns on the soft soil behavior during the tube's driving.

3.1. Evaluation of driving-induced displacements in a single-GEC system

Fig. 3 shows the distribution of lateral displacements (u) for M1S2 for a single GEC driven into the soft foundation soil where the upper scale is the horizontal distance (x) normalized by the tube radius (R) corresponding to the half the width of the model, the left scale is the soft foundation depth (z) normalized by the tube radius (R) corresponding to the depth of the model and the right colored scale indicates the

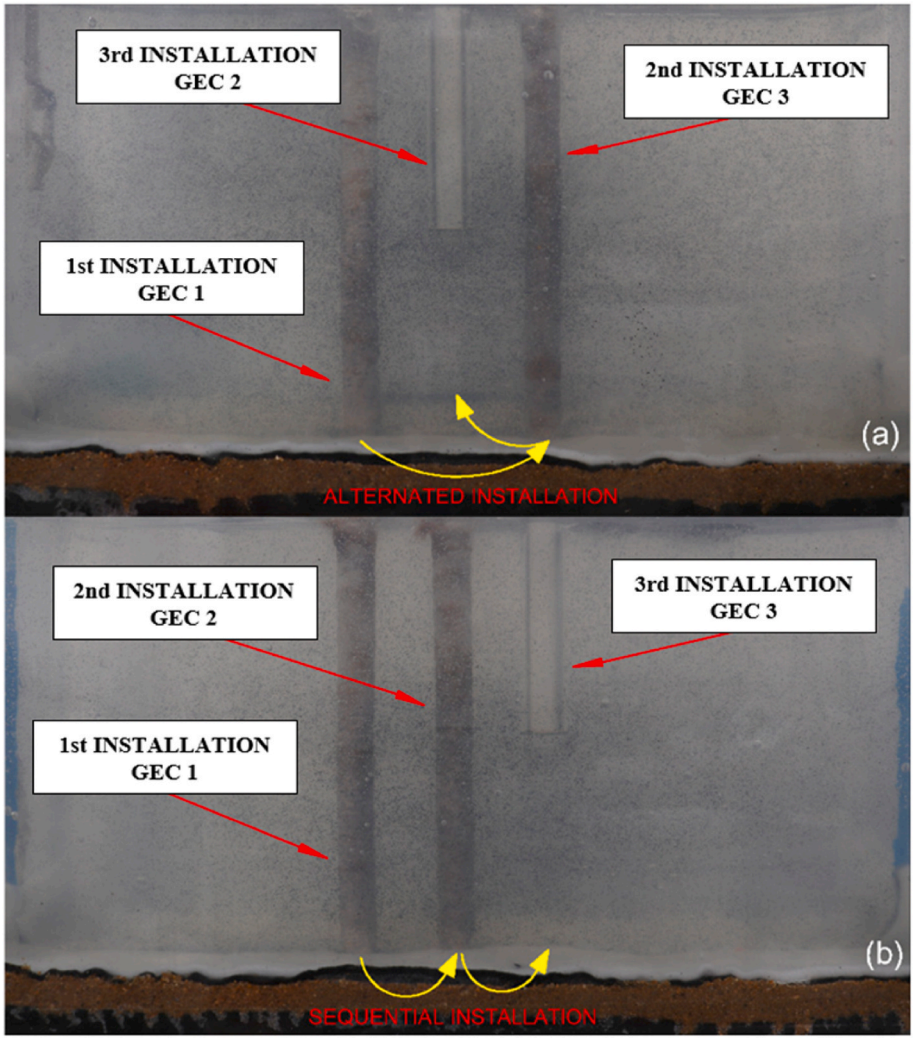

Fig. 2. Installation sequences considered: (a) Alternated and (b) Sequential.

cumulative lateral displacements (u) values within the soil foundation from the beginning to the current stage of driving. In the same Fig. 3, the distribution of lateral displacements was plotted for pile driving stages of 25 %, 50 %, 75 % and 100 %, referring to the ratio of the tube length driven to the total soft soil layer thickness. The black dashed lines in Fig. 3 indicate the location of a hypothetical neighboring GEC, considering a horizontal spacing between GECs of 2.0 m (prototype scale). The solid red line denotes the maximum spread curve characterized as the border region of the lateral displacements field originating during the tube's driving into the soft foundation soil, beginning on the tube's limits to the region where the lateral displacements remain visually well-defined and continuous (dark blue region), limited over the 0.16R displacement values under these conditions. The horizontal dashed white lines divide the maximum spread region into three simplified geometric forms to better understand the pattern of the displacements observed.

The lateral displacements in the soft soil caused by tube driving, as observed in Fig. 3, are significant, as they extend far enough to potentially affect adjacent columns spaced 2.0 m apart (in prototype scale) from the column being installed what provides evidence that lateral stresses may be transferred to adjacent GECs, a variable not considered in the design analysis. The maximum spread curve indicates that lateral displacement toward the neighboring GEC increased as tube driving progressed, resulting in shape pattern of lateral displacement distribution along the depth of the driven tube, extending beyond the neighboring GEC.

To assess the effects of tube driving, two key parameters related to displacement were analyzed. The first is the maximum displacement observed in the model, representing the peak values caused by tube driving. The second parameter is the maximum spread, defined by the maximum distance with clear pattern from the tube to the border region. Displacements after this region are diffuse and variable, with no pattern and great dispersion on its shape and values and are not considered for the maximum spread curve adjust.

To study the maximum spread curve of displacements originating from the tube driving, functions were developed to express a curve that denotes its spread, thereby capturing the installation's impact on neighboring GECs. These functions were developed to estimate the maximum spread curve at 25 %, 50 %, 75 % and 100 % of the tube's depth. The maximum spread was limited over the region where the lateral displacements values are close to 0.16R for the four analyzed driving stages. The area within this maximum spread region was divided into three standard geometric shapes to define the functions illustrated with red contours in Fig. 3 (a), (b), (c) and (d). Based on the shapes defined for the maximum spread curve, functionss were developed to describe each of the analyzed region: (i) the first segment at the upper portion of the tube is represented by a decreasing linear function (triangle); (ii) the second segment is a constant function describing the lateral displacement range, extending from the end of the first segment to the tube tip region (rectangle); and (iii) the final segment is an arc of a

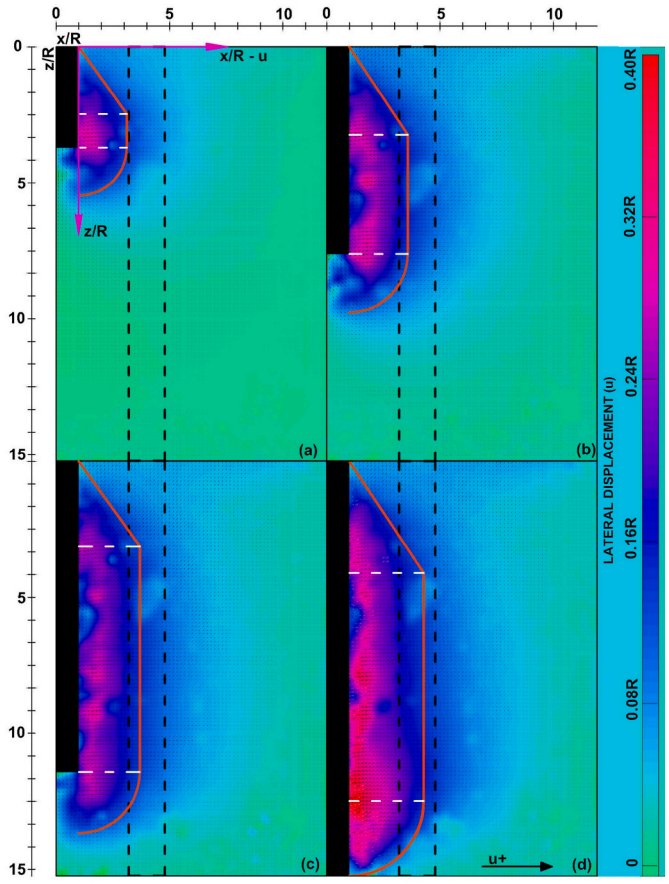

Fig. 3. Lateral soil displacement during tube penetration – M1S2 – u direction (D = 25.0 mm): (a) 25 %; (b) 50 %; (c) 75 %; and (d) 100 %.

circle, with a radius equal to the lateral displacement maximum spread value and its center located at the tube tip (arc of circumference). The functions were limited to the case herein analyzed considering just one group of materials and tube radius and aimed to provide an initial understanding of the displacements spread, needing further studies to be generalized. The center of the coordinate system was set to the top of the tube as indicated by the pink arrows.

The $x_{u,(\%)}$ presented in the Functions (2), (3), (4) and (5) describes the lateral displacements maximum spread curve for each stage of tube driving considered.

$$\frac{x_{u,25\%}}{R} = \begin{cases} \dfrac{z}{1.4R} & 0 \le \dfrac{z}{R} < 3 \\ 2.1 & 3 \le \dfrac{z}{R} < \dfrac{0.25L}{R} \\ \sqrt{4.54 - \left[\dfrac{z}{R} - \dfrac{0.25L}{R}\right]^2} & \dfrac{0.25L}{R} \le \dfrac{z}{R} \le \dfrac{0.25L}{R} + 2.1 \end{cases} \tag{2}$$

$$\frac{x_{u,50\%}}{R} = \begin{cases} \dfrac{z}{1.5R} & 0 \le \dfrac{z}{R} < 4 \\ 2.6 & 4 \le \dfrac{z}{R} < \dfrac{0.50L}{R} \\ \sqrt{6.76 - \left[\dfrac{z}{R} - \dfrac{0.50L}{R}\right]^2} & \dfrac{0.25L}{R} \le \dfrac{z}{R} \le \dfrac{0.50L}{R} + 2.6 \end{cases} \tag{3}$$

$$\frac{x_{u,75\%}}{R} = \begin{cases} \dfrac{z}{1.5R} & 0 \le \dfrac{z}{R} < 4 \\ 2.7 & 4 \le \dfrac{z}{R} < \dfrac{0.75L}{R} \\ \sqrt{7.30 - \left[\dfrac{z}{R} - \dfrac{0.75L}{R}\right]^2} & \dfrac{0.25L}{R} \le \dfrac{z}{R} \le \dfrac{0.75L}{R} + 2.6 \end{cases} \tag{4}$$

$$\frac{x_{u,100\%}}{R} = \begin{cases} \dfrac{z}{1.5R} & 0 \le \dfrac{z}{R} < 5 \\ 3.3 & 5 \le \dfrac{z}{R} < \dfrac{L}{R} - 3.3 \\ \sqrt{10.90 - \left[\dfrac{z}{R} - \dfrac{L}{R} - 3.3\right]^2} & \dfrac{L}{R} - 3.3 \le \dfrac{z}{R} \le \dfrac{L}{R} \end{cases} \tag{5}$$

where L is the total column length; z is the depth under consideration; and R is the tube radius. The proposed functions were derived from the results of M1S2 and tested on a duplicate model, achieving good fit. Fig. 3 also illustrates the maximum spread curve fitted for M1S2 in accordance with the functions obtained for the four driving stages.

The maximum lateral displacements observed on the soft foundation during the GEC installation reached values near 0.40R and remained concentrated in the region close to the tip of the tube, spreading over up to 1R in relation to the side of the tube. Along the maximum spread, as described before, the values were approximately 0.16R. In M1S2, this value reached 2.1R at 25 % of driving, increasing to about 3.3R at 100 % of driving. The intermediate stages, at 50 % and 75 % of driving, showed similar trends, with maximum values of 2.6R and 2.7R, respectively.

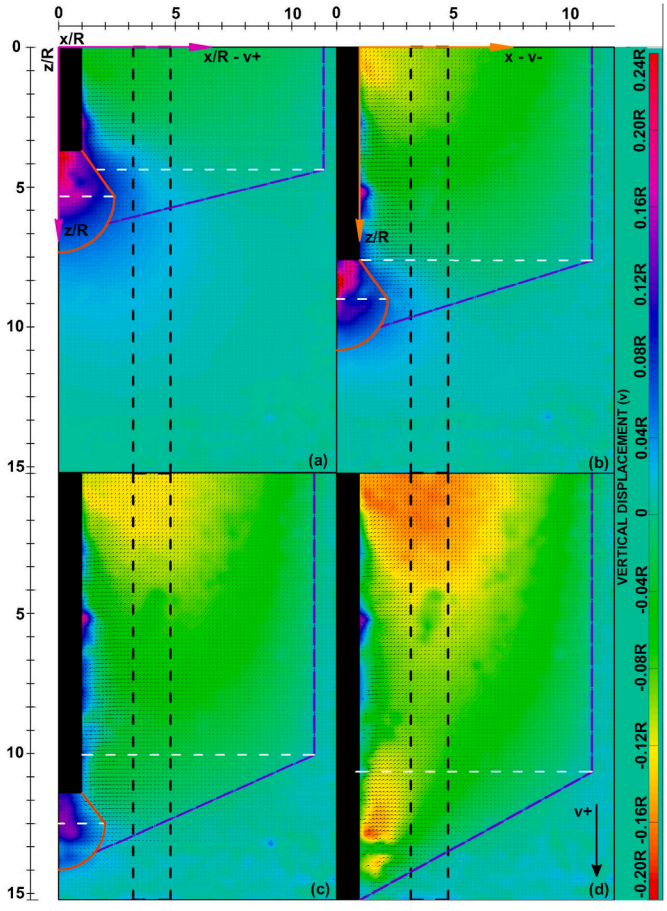

Fig. 4. Vertical soil displacement during tube penetration – M1S2 – v direction (D = 25.0 mm): (a) 25 %; (b) 50 %; (c) 75 %; and (d) 100 %.

The next analysis was centered on the vertical displacements in the soft foundation soil caused by tube driving. Fig. 4 shows the vertical displacements within the transparent soil on M1S2 regarding the same four stages of driving (25 %, 50 %, 75 % and 100 %). The solid black rectangle in Fig. 4 represents the tube, the dashed line rectangle is the neighboring GEC, the upper scale is the horizontal distance (x) normalized by the tube radius (R) corresponding to the half the model width, the left scale is the soft foundation depth (z) normalized by the tube radius (R) corresponding to the model and depth the right colored scale indicates the vertical displacements (v) values within the soil foundation from the beginning to the current stage of driving. The main difference in this case is that two maximum spread curves were defined for vertical displacements as the soil moves downward and upward depending on the region of analysis. The red solid line is the maximum spread curve for downward displacements and the purple line for the upward displacements. The displacements over this curve were near 0.16R (downward) and −0.04R (upward). The premise used to construct the curve was the same as in the previous case with the white dashed lines dividing the curves into simplified geometric shapes. The limitations of the functions are the same as those discussed previously and can't yet be generalized to other cases.

The DIC analyses show that the maximum downward vertical displacements occurred right below the tip of the driving tube after the formation of a displacement bulb due to the soft soil compression. Over the four driving stages, vertical displacements were highest at 25 % driving, with maximum values exceeding 0.30R at the center of the bulb under the tube's tip. The maximum spread curve (red line) with 0.16R values reached a maximum vertical distance of 4.2R under the tube tip. The initially higher and localized displacements observed beneath the tip at 25 % driving tube may be attributed to the greater shear stresses mobilized to overcome the tip resistance, which decreased as driving progressed. Additionally, the formation of the bulb of displacements under the tip contributed to lateral soil mobilization, also contributing to the propagation of the lateral displacements analyzed previously.

In the stages of 50 % and 75 % driving, the bulb became smaller, with the vertical displacements spread curve maximum vertical distance under the tube tip decreasing to 3.5R and 3.0R, respectively. During these stages, the tube punched down through the soft soil and skin friction became dominant laterally mobilizing the material until driving ceased at 100 % of driving. The vertical displacements along the tube's sidewall correspond to soft foundation soil mobilized by skin friction, which is dragged downward, forming a smeared region adjacent to the tube's side. This process is comparable to the driving of a conventional pile with a circular cross-section as described by Massarsch. and Wersäll (2013).

Functions to quantify the downward vertical displacements (positive direction) were developed following a similar approach to that used for lateral displacements, where the bulb's maximum spread curve was divided into two simplified geometric shapes. The curve was plotted within the dark blue region on the 0.08R lateral displacements values, which define the bulb's maximum spread. The upper region of the bulb can be represented by a triangle, beginning at the tube's tip and extending to the boundaries of the next area. The second region was modeled as an arc of circumference with its center at the tube tip. Functions (6), (7), and (8) present simplified expressions for estimating the downward vertical displacements maximum spread (x_{v^+}) beneath the tube tip for the first three driving stages. The origin is located at the center of the tube at the top surface of the tube and indicated by pink arrows. Displacements mobilized by skin friction near the tube wall were not considered on the functions because they were not clearly defined in the images, were discontinuous along the depth, and had low values. The downward vertical displacements maximum spread curve (red line) was divided into two regions: (i) a decreasing linear function with a fixed slope and (ii) a circumferential arc. Also, the functions define the bulb's maximum spread curve horizontal position from the tube's side ($x_{v^+,\%}$).

$$\frac{x_{v^+,25\%}}{R}=\begin{cases} R+\dfrac{z}{1.4R}-\dfrac{0.25L}{1.4R} & \dfrac{0.25L}{R}\le\dfrac{z}{R}<\dfrac{0.25L}{R}+2 \\ \sqrt{5.76-\left[\dfrac{z}{R}-\dfrac{0.25L}{R}-2\right]^2} & \dfrac{0.25L}{R}+2\le\dfrac{z}{R}\le\dfrac{0.25L}{R}+4.4 \end{cases} \tag{6}$$

$$\frac{x_{v^+,50\%}}{R}=\begin{cases} R+\dfrac{z}{1.4R}-\dfrac{0.5L}{1.4R} & \dfrac{0.5L}{R}\le\dfrac{z}{R}<\dfrac{0.5L}{R}+1.7 \\ \sqrt{4.84-\left[\dfrac{z}{R}-\dfrac{0.5L}{R}-1.7\right]^2} & \dfrac{0.5L}{R}+1.7\le\dfrac{z}{R}\le\dfrac{0.5L}{R}+3.9 \end{cases} \tag{7}$$

$$\frac{x_{v^+,75\%}}{R}=\begin{cases} R+\dfrac{z}{1.3R}-\dfrac{0.75L}{1.3R} & \dfrac{0.75L}{R}\le\dfrac{z}{R}<\dfrac{0.75L}{R}+1.3 \\ \sqrt{4.00-\left[\dfrac{z}{R}-\dfrac{0.75L}{R}-1.3\right]^2} & \dfrac{0.75L}{R}+1.3\le\dfrac{z}{R}\le\dfrac{0.75L}{R}+3.3 \end{cases} \tag{8}$$

The variables are the same as the Functions (2), (3), (4) and (5).

A second analysis of vertical displacements focused on the upward movement of material during tube driving, which primarily affected the upper region of the model. The maximum upward vertical displacement values reached significant magnitudes near 0.20R and were observed over the neighboring GEC region next to the soft foundation soil surface. This behavior aligns with results reported by Massarsch. and Wersäll (2013) for concrete pile driving. Initially, the soft soil was displaced laterally (in a trapezoidal region) by the tube and the bulb shaped vertical displacements field formed under the tip and may increase stresses in the area adjacent to the tube. Subsequently, the soil moved upward, resulting in displacements within the orange region (Fig. 4). During most of the tube driving stages adopted, these upward displacements reached the neighboring GEC region, indicating that the soft soil mobilized in this direction during driving may affect this adjacent column.

The functions for the four penetration stages corresponding to upward displacements maximum spread curve ($x_{v^-,\%}$) are presented in Functions (9), (10), (11) and (12), and are represented by the purple dashed line in Fig. 3. In this analysis, the boundary region spread curve was divided into two regions, with orange arrows indicating the origin. The first region is a constant function that describes the displacements maximum spread from the tube and is represented by a rectangle. The second region is a crescent-shaped linear function that begins near the tube tip with a constant slope, corresponding to a triangular shape. The premise adopted was the same used in the previous cases but $x_{v^-,\%}$ we're not normalized by the radius as the normalization impacted on the adjusted curves dispersion in the models considered for the function deduction.

$$x_{v^-,25\%}=\begin{cases} \dfrac{5.2}{R} & 0\le\dfrac{z}{R}<\dfrac{0.3L}{R} \\ \dfrac{5.2}{R}-4\dfrac{z}{R}+1.2\dfrac{L}{R} & \dfrac{0.3L}{R}\le\dfrac{z}{R}\le\dfrac{0.3L+1.3}{R} \end{cases} \tag{9}$$

$$x_{v^-,50\%}=\begin{cases} \dfrac{5.0}{R} & 0\le\dfrac{z}{R}<\dfrac{0.5L}{R} \\ \dfrac{5.0}{R}-\dfrac{10}{3}\dfrac{z}{R}+\dfrac{5}{3}\dfrac{L}{R} & \dfrac{0.5L}{R}\le\dfrac{z}{R}\le\dfrac{0.5L+1.5}{R} \end{cases} \tag{10}$$

$$x_{v^-,75\%}=\begin{cases} \dfrac{5.0}{R} & 0\le\dfrac{z}{R}<\dfrac{0.68L}{R} \\ \dfrac{5.0}{R}-\dfrac{20}{9}\dfrac{z}{R}+1.51\dfrac{L}{R} & \dfrac{0.68L}{R}\le\dfrac{z}{R}\le\dfrac{0.68L+2.25}{R} \end{cases} \tag{11}$$

$$x_{v^-,100\%} = \begin{cases} \dfrac{5.0}{R} & 0 \le \dfrac{z}{R} < \dfrac{L-3}{R} \\ \dfrac{5}{3}\left(\dfrac{L}{R} - \dfrac{z}{R}\right) & \dfrac{L-3}{R} \le \dfrac{z}{R} \le \dfrac{L}{R} \end{cases} \quad (12)$$

where L is the column length; z is the position depth; and R is the tube radius (all units are in meters [m]). In this final case, the maximum spread curve higher is observed to be approximately equal across the four scenarios. The behavior observed for all the displacements is consistent with the existing literature (Engin et al., 2015; Arif and Potgieter, 2016; Fakharian and Khanmohammadi, 2022).

3.2. Evaluation of driving-induced displacements in a GEC group with different spacings

In this section, test configurations were selected to examine the effect of GEC installation on a previously installed GEC, considering different horizontal spacings of 1.0 m (2R), 1.5 m (3R), 2.0 m (4R), and 2.5 m (5R) center-to-center at the prototype scale. This analysis focused on the 50 % and 100 % driving stages as these exhibit the most impacting displacements on the soft foundation over the neighboring GEC during the installation process. In Fig. 4, the black rectangle represents the tube being driven and the yellow rectangle a previously installed GEC. During the tube's driving, the neighboring GEC trend to suffer some strain due to the soft foundation displacements, changing its geometry. In this case, the deflection observed on the neighboring GEC at each stage is depicted by the solid red line drawn beside the column. The black arrows show the positive direction of displacements.

As can be observed in Fig. 5, the highest lateral displacement values noticed at 50 % driving were similar for all the four models studied with values ranging from 0.16R to 0.24R. However, the distribution and spread of these higher displacements field decreased as the spacing between columns increased. For the critical case of S = 1.0 m (M2S1), these higher displacements extended to approximately 3R beyond the tube's limits, even with the limitation provided by the previously installed column. The displacements observed adjacent to the neighboring GEC indicate their movement, represented by the deflection curve, resulting from the soft soil displacements caused by the tube's driving. As the spacing values increased, these higher displacements became increasingly confined to the region between the GEC and the tube, reducing their influence on the previously installed column.

Nonetheless, still in the 50 % driving stage, the maximum spread in M2S1(Fig. 5-a), M2S1.5 (Fig. 5-b) and M2S2 (Fig. 5-c), defined over the 0.08R lateral displacements value, showed a larger spread extending beyond the neighboring GEC's region on these three models. In the intermediate cases (M2S1.5 and M2S2, the lateral displacements maximum spread also revealed some strain experienced by the neighboring column, although their effect was less pronounced compared to M2S1, the critical case. In the final case (M2S2.5), lateral displacements maximum spread had a reduced effect on the neighboring GEC because of its confinement to the region near the tube, maintaining a distance of approximately 1.5R from the neighboring column (Fig. 5-d). The reduction in the GEC curves deflection as the spacing between the columns increase clearly demonstrates that increasing the distance between columns effectively mitigates the displacements effects on the surrounding columns in up to 60 % comparing M2S1 and M2S2.5, the opposite extreme cases.

Regarding vertical displacements at the 50 % driving stage (Fig. 6), the same bulb of displacements was observed under the tube's tip, although its spread is conditioned by the column spacing. In the case of M2S1(Fig. 6-a), the reduced spacing laterally confined the bulb, which led to higher and more concentrated maximum downward vertical displacements (approximately 0.32R) and, consequently, higher displacements over the preexisting column. This situation may contribute to slight deflection of the GEC as indicated by the strain line. In M2S1.5 (Fig. 6-b), the bulb also experienced lateral restriction, though less intense in the previous case -, with maximum downward vertical displacements of around 0.16R. For the last two cases, M2S2 (Fig. 6-c) and

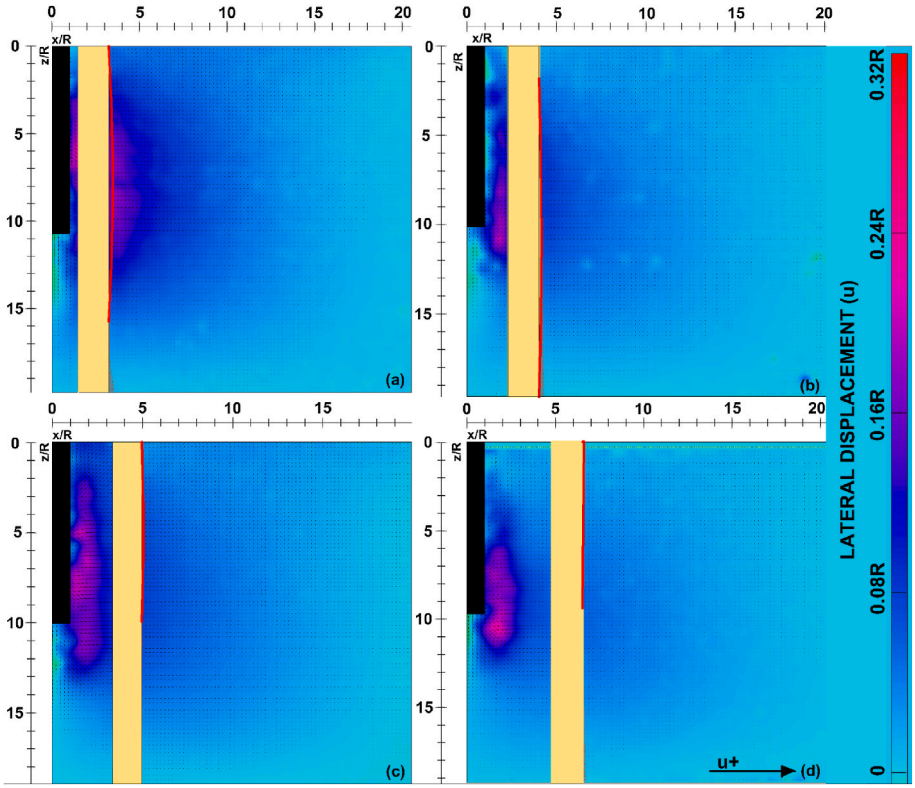

Fig. 5. Soil displacement during tube driving – 50 % of driving – u direction: (a) M2S1(S = 1 m); (b) M2S1.5 (S = 1.5 m); (c) M2S2 (S = 2 m); and (d) M2S2.5 (S = 2.5 m).

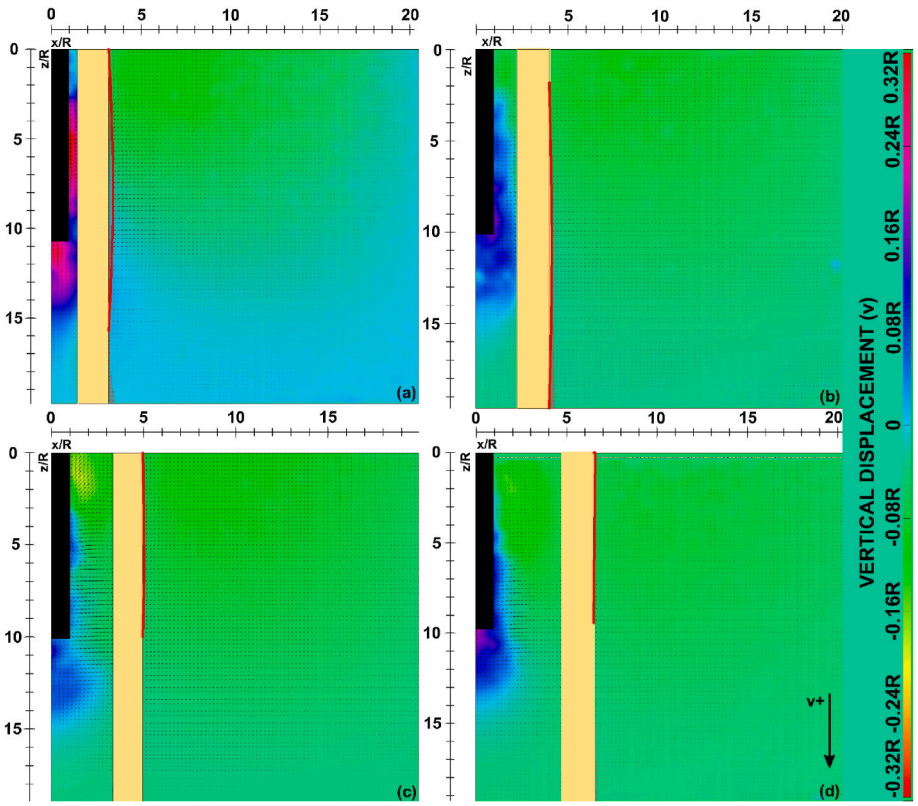

Fig. 6. Soil displacement during tube driving – 50 % of driving – v direction: (a) M2S1(S = 1 m); (b) M2S1.5 (S = 1.5 m); (c) M2S2 (S = 2 m); and (d) M2S2.5 (S = 2.5 m).

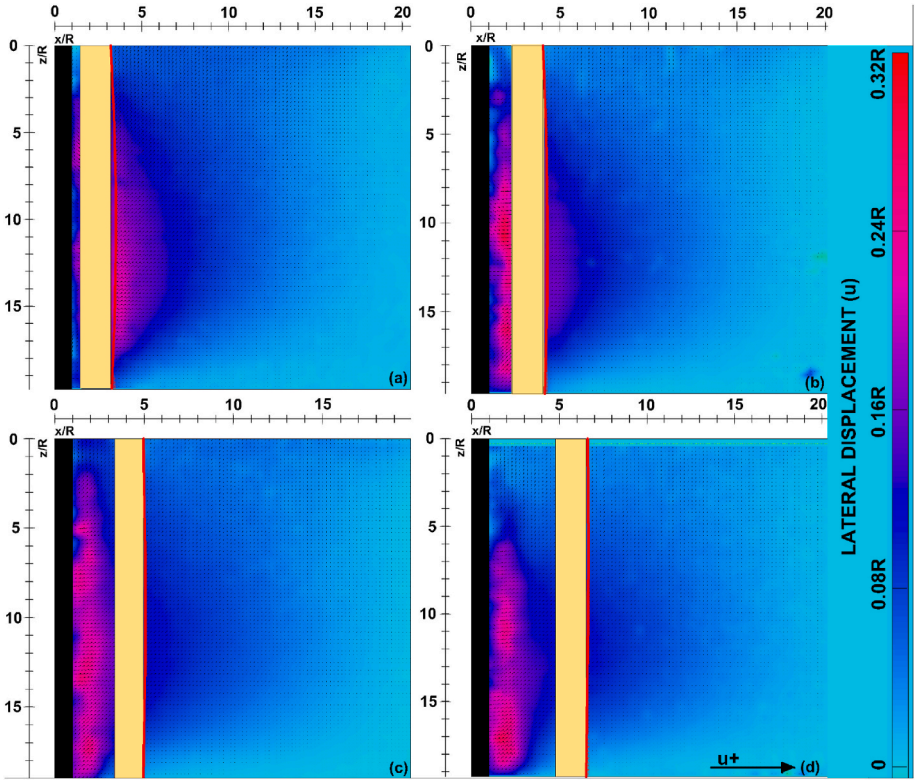

Fig. 7. Soil displacement during tube driving – 100 % of driving – u direction: (a) M2S1 (S = 1 m); (b) M2S1.5 (S = 1.5 m); (c) M2S2 (S = 2 m); and (d) M2S2.5 (S = 2.5 m).

M2S2.5 (Fig. 6-d), the bulb of displacements beneath the tube tip was less pronounced, with maximum values reaching up to only 0.10R as the increased spacing reduced the confining effect of the GEC. This represents a 69 % reduction in downward vertical displacements in M2S2.5 compared to M2S1. Nonetheless, the bulb of displacements continued to influence soil lateral displacements, spreading over an average vertical distance of 5R under the tube's tip.

The negative vertical displacements (upward) were more pronounced on the right side of the model and are consistent with the behavior described by Massarsch. and Wersäll (2013), where soil located farther from the tube undergoes an upward movement toward the surface after being displaced laterally. The average value in this case was approximately 0.08R. However, the spread of these displacements' fields may be limited by the neighboring GEC, particularly at smaller spacing values as observed in M2S1 (Fig. 6-a). In this case, the displacement field on the right side was concentrated in the upper region of the soil. As spacing increased, the range of these displacement fields decreased because the soft soil movement experienced less restriction.

Fig. 7 shows the lateral displacements for 100 % of tube driving for the four spacing considered. The elements on Fig. 7 are the same introduced previously in Figs. 5 and 6. After the driving process was completed (100 % of driving), the installation effects on the neighboring GEC became notable as the lateral displacement field (Fig. 7) affected the preexisting column in all the four models, with the maximum spread reaching the 0.08R values region significantly influenced by the spacing between the tube and neighboring GEC. As previously mentioned, M2S1 (Fig. 7-a) represents the critical case, where the proximity of the tube led to higher displacements on the neighboring GEC. The higher lateral displacements on the right side of the neighboring GEC reached values of up to 0.32R and spread across a large area along the length of this column. The deflection on the neighboring GEC is clearly visible on the deflection curve drawn on the right side of the column and aligns with the shape of the lateral displacement propagation. Lateral displacements were observed, even at distances of 6R beyond the GEC limits, with values close to 0.10R. A slight deflection was evident at smaller spacings, mainly on M2S2 (Fig. 7-c) and M2S2.5 (Fig. 7-d). However, in practice, this deflection may be mitigated by the installation of another GEC on the opposite side, which may push the element back into place.

Increasing the spacing to 1.5 m (M2S1.5 see Fig. 7-b) reduced the effect of lateral displacements, although maximum displacements of up to 0.32R were still observed on the right side of the previous GEC but spread over a smaller area compared to M2S1 (Fig. 7-a). The neighboring GEC also experienced some deflection at mid-depth, though to a lesser extent than in the previous case. In this scenario, the lateral displacement maximum spread curve reaches areas as far as 6R from the GECs side. For the two final cases, M2S2 (Fig. 7-c) and M2S2.5 (Fig. 7-d), higher lateral displacements value up to 0.32R remained concentrated in the region between the tube and column, with reduced influence over the neighboring GEC.

The distribution of negative vertical displacements (upward) on the right side of the neighboring GEC, with average values around 0.08R, maintained the same pattern at the end of the tube's driving and spread over almost the entire length of the GEC (Fig. 8). After undergoing a lateral displacement, the soft soil moved upward toward the surface, beginning at the lower section of the neighboring GEC. In this case, the higher vertical displacements were observed in the region of the soft foundation between the tube and preexisting column, primarily in the upper and lower ends. Values up to 0.24R were recorded in these regions and may be attributed to the reduced space, which directs the material upward. This behavior is consistent across all four spacing scenarios considered.

Based on the results for two columns models, it is evident that spacing has a significant effect during the driving process. Greater spacing can reduce the effects of soft soil movement on the neighboring GEC, thereby mitigating the deflection on these elements. During

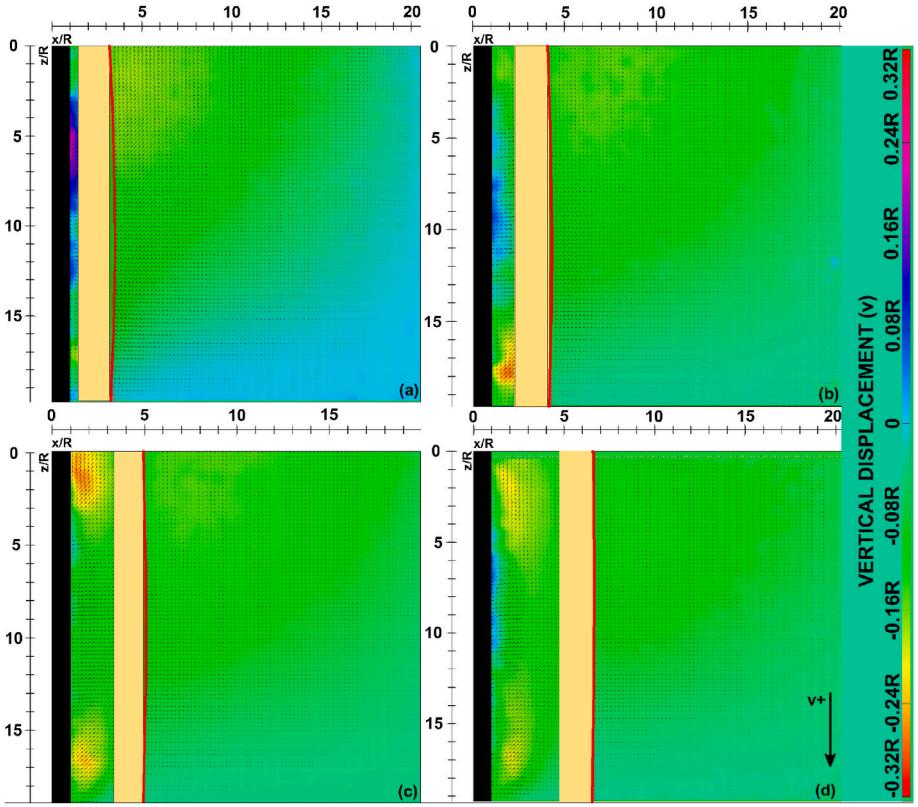

Fig. 8. Soil displacement during tube driving – 100 % of driving – v direction: (a) M2S1 (S = 1 m); (b) M2S1.5 (S = 1.5 m); (c) M2S2 (S = 2 m); and (d) M2S2.5 (S = 2.5 m).

driving, the primary variation observed was the spread of the lateral field displacements, which is strongly influenced by changes in spacing. However, increased spacing can significantly reduce bearing capacity depending on field conditions such as embankment height and stiffness (Fattah et al., 2016; Hanna et al., 2019; Al-Kazzaz and Al-Obaydi, 2021). Therefore, careful evaluation and balancing of these two variables are essential during the design process. Unlike M1S2, the field displacements observed in the two-column models exhibited larger ranges that extended even beyond the first installed GEC. This indicates that lateral displacements are the most critical factor in studying GEC installation, although vertical displacements also contribute to their propagation.

These findings align with the study by Zhou et al. (2021), which examined the response of installed piles during the driving of a new one. Although concrete piles exhibit higher stiffness compared to GECs, they still experience slight soil-induced deflection, which becomes more pronounced as spacing is reduced. Nevertheless, it is not possible to conclude that all lateral displacements observed adjacent to the columns are directly linked to column bending as soft soil can move around the GEC and continue its lateral motion on the other side.

Observations of lateral displacements adjacent to the right side of the neighboring GEC (u_b) confirm that increasing the spacing reduces the influence of lateral displacements on the element for all stages of driving (Fig. 9-a). When comparing M2S1 and M2S2.5, a reduction of approximately 50 % in lateral displacements beside the neighboring GEC was

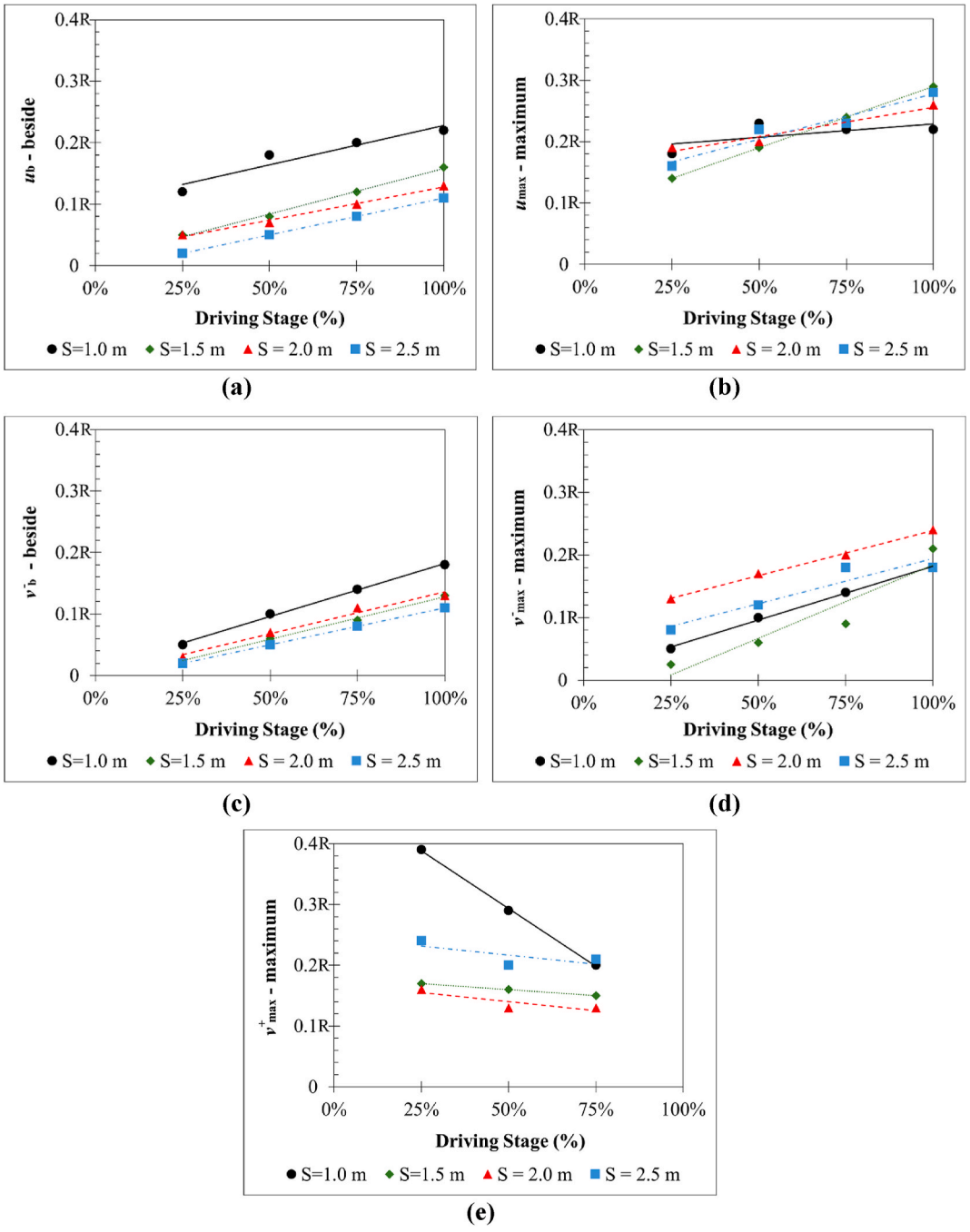

Fig. 9. Soil displacement during tube driving: (a) lateral displacements at right side of the neighboring GEC; (b) maximum lateral displacement values; (c) upward vertical displacements at right side of the neighboring GEC (right side); (d) maximum upward vertical displacement values; and (e) maximum downward vertical displacement values.

observed at the end of installation, which also indicates reduced deflection on the element. Smaller spacings restrict soft soil movement and increase displacements over the neighboring column as the tube driving compresses the soft soil toward it. For a given spacing, the lateral displacements beside the GEC are expected to increase as installation progresses, a trend observed for all spacing values analyzed in this investigation. When focusing only on the maximum lateral displacements (u_{max}), no clear trend related to spacing variation emerged as M2S1.5 exhibited values higher than those for other spacings at the end of tube driving (Fig. 9-b). For M2S1, the values remained nearly constant after 25 % of tube driving, which can be attributed to the higher confinement that limits soil movement. In contrast, for longer spacings, the maximum lateral displacements trended to increase as installation progressed. The spacing S = 1.5 m showed the greatest variation, with values increasing by nearly 110 % from 25 % to 100 % of tube driving. This variability in maximum lateral displacements may stem from differences between models and the DIC analysis process. As previously stated, while increased spacing can reduce the installation's influence on neighboring GECs, it must be carefully considered. Although beneficial for mitigating effects on other GECs, increased spacing may also reduce the system's overall bearing capacity.

When considering the upward vertical displacements at the right side of the neighboring GEC (v_b^-), the values in this region tend to reduce with the increase in spacing (Fig. 9-c). For S = 2.5m (M2S2.5), these values were reduced by nearly 39 % when compared with the results from M2S1 at the end of tube driving (100 %). Observing the other driving stages, it is possible to verify slightly higher values for M2S2 when compared to M2S1.5, interrupting the expected decrease. But this behavior may be associated do the variability in the models and the result can be considered practically equal. For the maximum values for this type of displacement (v_{max}^-) (Fig. 9-d), it is difficult to identify a pattern, as the displacements increase from S = 1.0 m–2.0 m (33 %) and then decrease 25 % for S = 2.5 m, considering the end of the driving (100 %). The other driving stages show more variable results, where the values decrease from S = 1.0 m to S = 1.5 m, increase for S = 2.0 m, then decrease again for the higher spacing. This again may be linked to the model's variability or the higher value of spacing induces a lower concentration of displacements at the end of the drive. Restricting the analysis to a same spacing, the upward displacements values increase as the tube driving advances for the two kinds of displacements availed.

Fig. 9-e shows that the maximum downward vertical displacements (v^+_{max}) were greatest at 25 % of tube driving for all spacing values, similar to the trends observed in M1S2. In this case, the presence of a neighboring GEC played a significant role by confining the soft soil in the region between the tube and column. The behavior depends on the spacing distance. M2S1 represents the most critical case because the proximity of the GEC (smaller spacing) limited lateral displacements and forced the soil to move downward. As a result, the maximum downward vertical displacements for M2S1 were 66 % larger than those observed in M1S2, where no GEC was installed. This demonstrates the importance of including a real GEC in the analysis and the limitations of excluding it. Additionally, M2S1 showed the highest maximum value compared to the other three spacing distances, emphasizing its critical influence on the neighboring GEC. In contrast, the results for M2S1.5, M2S2 and M2S2.5 were less conclusive relative to displacement direction. Displacement values showed a decreasing trend for S = 1.5 and S = 2.0 m compared to M2S1 but increased again considering S = 2.5 m. This may be due to model variability and DIC analysis. When the same spacing was maintained, downward vertical displacements tended to decrease as driving progressed, aligning with observations from the initial model type. Despite this, the same bulb shape, caused by soft soil compression under the tip, remained consistent across all models and showed similar behavior throughout the range of cases.

Analysis of all models indicates that lateral displacements have the most significant effect on the surrounding area, as the model evaluations demonstrated. Considering the effect of these displacements on neighboring GECs it becomes evident that maintaining a sufficient initial distance from other columns and structures before installation is essential. As observed earlier, a spacing of 2 m (4R) resulted in minimal displacements adjacent to the neighboring GEC, and these displacements tended not to change as spacing increased. Therefore, to reduce the effect of lateral displacements on nearby critical elements (such as other columns or structures), a minimum initial distance of 4R should be maintained between the tube and these elements during installation.

3.3. Evaluation of induced displacements in a GEC group with varying driving patterns

The models involving the installation of three GECs were analyzed under two different configurations, both with 2.0 m spacing. In the first configuration (M3S2A), the odd-numbered columns (the first and third GECs) were initially installed, followed by the middle column between them (1-3-2 sequence), a sequence commonly employed in practice. In the second configuration (M3S2S), all three columns were installed in row (1-2-3 sequence). The two sequences of installation were depicted previously on Fig. 2. This analysis aimed at comparing the effectiveness of these two configurations to minimize overall displacements both within and alongside the GECs during tube driving. In M3S2A, only the installation of the last two GECs was analyzed as the single-column case was examined previously. Conversely, in M3S2S, only the last installation was evaluated because the results from the first two installations closely resembled those observed in the M2S2 case. Furthermore, only the 50 % and 100 % driving stages were considered under the same analysis pattern used in the previous case. The elements in the images remained unchanged except for the deflection curve shown beside the GECs.

Fig. 10 shows the lateral displacements mobilized on the soft foundation soil during the installation of GECs 3 and 2 in M3S2A for 50 % and 100 % of tube driving. During the installation of GEC 3 (Fig. 10-a), the second column in the sequence, the larger initial spacing between the first two columns in the M3S2A configuration (approximately 4.0 m at the prototype scale or 8R) reduced the effect of soil movement on the first installed GEC (on the left). This is because the large spacing allowed soil movement with minimal restriction. Nonetheless, GEC 1 experienced a reduced deflection by the end of the installation process (Fig. 10-b), as confirmed by the displacement field on the soft foundation soil on its left side. The maximum lateral displacements observed in the model increased from 0.24R at 50 % of driving (Fig. 10-a) to approximately 0.36R at 100 % driving (Fig. 10-b) on both sides of the tube, representing an increase of about 13 % during the installation of GEC 3.

During the installation of GEC 2 (the third column in the sequence), the tube driving had a more pronounced effect on the neighboring GECs, where the soft soil exhibited higher displacements (Fig. 10-c and 10-d). The confinement provided by GEC 1 and GEC 3 reduced lateral displacements, lowering the maximum value to 0.30R at 100 % tube penetration. This represents a 29 % reduction compared to the maximum displacements observed during the installation of GEC 3, where the foundation was freer to move. Furthermore, these maximum displacements were more localized and concentrated near the tube tip. However, lateral displacements began to emerge between the two prior GECs after 50 % tube driving, reaching values of approximately 0.10R at distances up to 3R from both GEC 1 and GEC 3. At 100 % of driving, these displacements increased to values of up to 0.13R, indicating movement in the GECs as observed in the deflection curve.

The vertical displacements (Fig. 11) exhibited a similar trend to those observed in previous models, forming a bulb-like shape of displacements beneath the tube tip. This maximum bulb spread decreased as driving progressed. At 50 % of driving, the maximum downward vertical displacement remained near 0.36R and in the middle region of the bulb of displacements (Fig. 11-a). Conversely, at 100 % driving, the maximum upward vertical displacement reached 0.19R (Fig. 11-b). Additionally, upward vertical displacements as high as 0.10R were

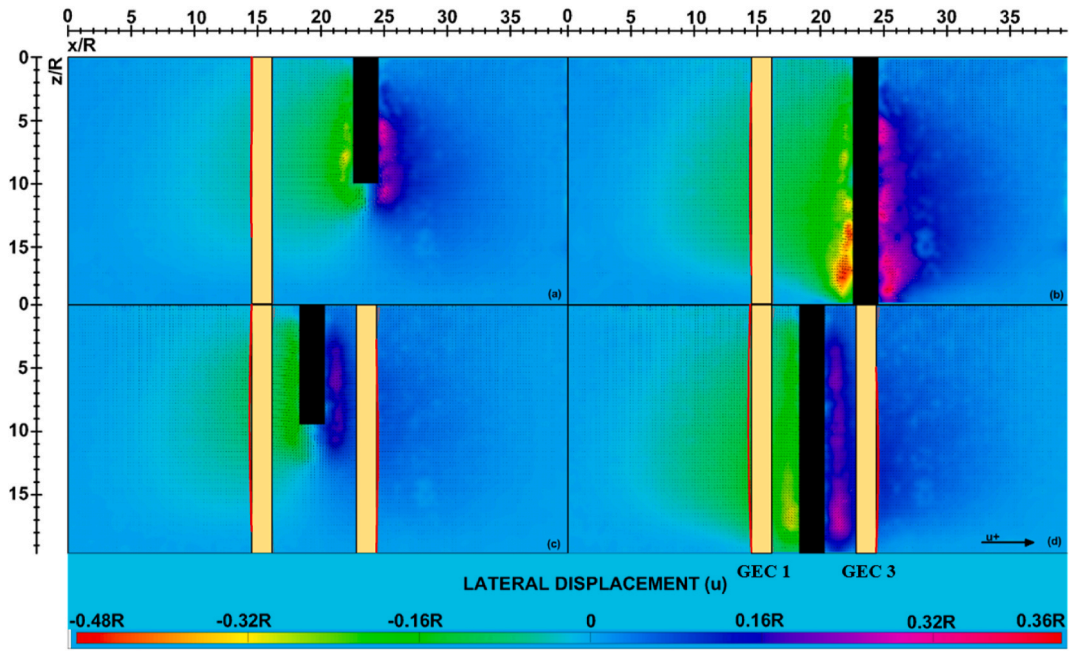

Fig. 10. Soil lateral displacement during GEC installation – u direction (S = 2 m): (a) M3S2A – GEC 3 installation - 50 % of driving; (b) M3S2A – GEC 3 installation - 100 % of driving; (c) M3S2A – GEC 2 installation - 50 % of driving; and (d) M3S2A – GEC 2 installation - 100 % of driving.

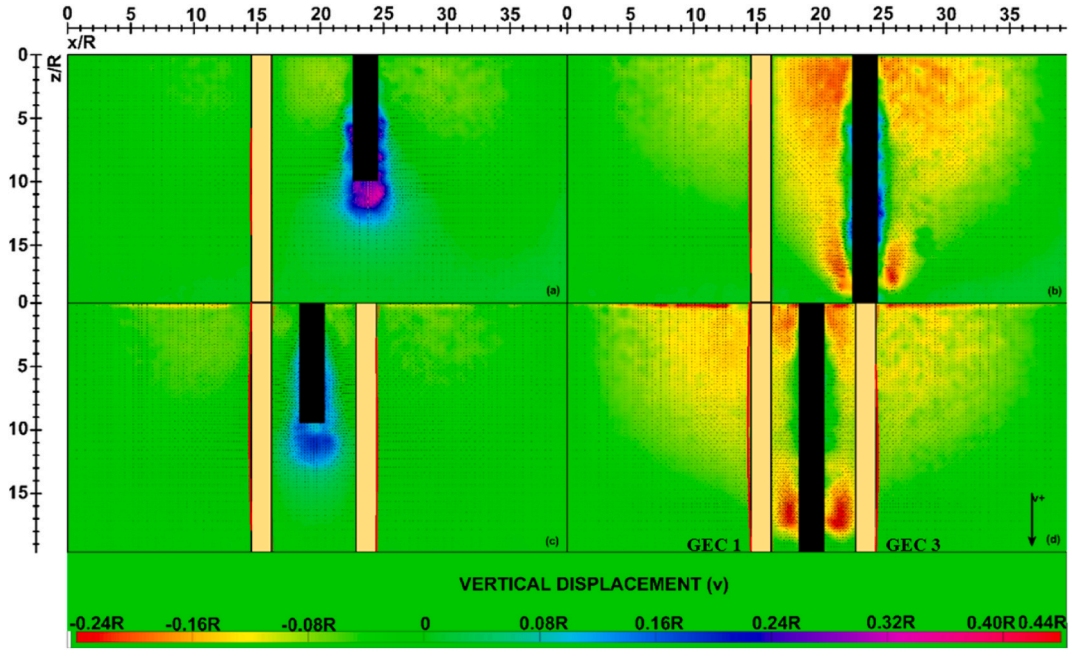

Fig. 11. Soil vertical displacement during GEC installation – v direction (S = 2 m): (a) M3S2A – GEC 3 installation - 50 % of driving; (b) M3S2A – GEC 3 installation - 100 % of driving; (c) M3S2A – GEC 2 installation - 50 % of driving; and (d) M3S2A – GEC 2 installation - 100 % of driving.

observed on the left of GEC 1 despite the larger initial spacing.

The downward vertical displacements within the bulb of displacements formed under the tube tip showed a significant reduction due to the restriction in space provided by the two GECs. These displacements decreased from about 0.36R to 0.19R, representing a 47 % reduction (Fig. 11-c and 11-d) when comparing the GEC 3 and GEC 2 installations. In terms of upward vertical displacements, the maximum values remained confined within the region between the first two GECs and the tube, reaching 0.24R, similar to the values observed during the GEC 3 installation. Additionally, upward displacements of 0.14R extended over a wider area, reaching locations as far as 10R away from both GECs 1 and 3 (Fig. 11-d). The soft soil movement near GECs 1 and 3 resulted in slight movements during tube driving as shown by the deflection curves.

The second test sequence involved the in-row installation of three GECs (1-2-3) under the M3S2S configuration. The assessment of this session focused solely on GEC 3, since the results from GECs 1 and 2 were similar to those observed in the previous models (M1S2 and M2S2) and were therefore excluded from further detailed analysis. Fig. 12 depicts lateral and vertical displacements during the installation of GEC 3, the last one in the row, for 50 % and 100 % tube driving in M3S2S. All the elements remained the same as observed in previous figures. During the GEC 3 installation, the maximum lateral displacements observed

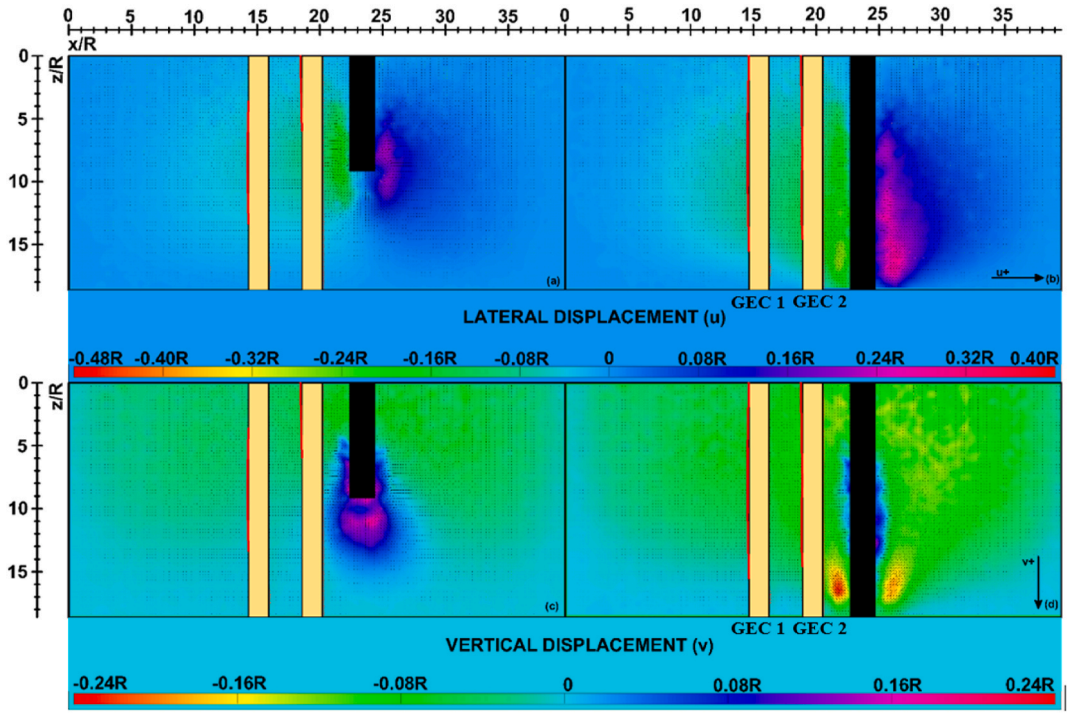

Fig. 12. Soil displacement during third GEC installation – M3S2S (S = 2 m): (a) 50 % of tube driving - u direction; (b) 100 % of tube driving - u direction; (c) 50 % of tube driving - v direction; and (d) 100 % of tube driving - v direction.

over the two existing columns (GECs 1 and 2) at 100 % of driving were lower compared to the last installation of the previous sequence (GEC 2 on M3S2A), with values near 0.27R, representing a 10 % reduction (Fig. 12-b). This reduction may be attributed to the higher stiffness provided by the two existing columns on the left side.

Despite being located at a greater distance and shielded by GEC 2, the first column installed (GEC 1) still exhibited lateral displacements on its left side with average values of 0.08R. This demonstrates that the influence of GEC installation persists even at considerable distances from the tube (8.5R), although the noticed values are considered low. Furthermore, during the GEC 3 installation, lateral displacements were observed on the left side of GEC 2, with average values near 0.12R. These displacements appear to be more strongly influenced by the movement induced by the tube's driving over the soft foundation soil. For both downward and upward vertical displacements (Fig.s 12-c and 12-d), the magnitudes and maximum spreads observed were consistent with those observed previously for M2S2, indicating replication of the same displacement patterns.

In summary, the two analyzed installation sequences exhibited distinct results, and their application depends on the intended objectives of the GEC deployment. The first configuration (M3S2A), where the columns were executed in an alternate order (1-3-2), favors greater displacements over the GECs in both the lateral and vertical directions. This directly affects the first two columns as they are near the tube. Additionally, this sequence leads to higher displacement values distributed over a larger area between the elements and tube, affecting different regions of the columns.

On the other hand, in the second configuration (1-2-3, M3S2S), the sequential GEC installation provides a gradual shielding effect over the previous columns installed, thereby limiting soil movement during the tube driving process (Fig. 12). The maximum lateral displacements observed over the GECs during the final installation (Fig. 12-b) were smaller than those in the M3S2A (Fig. 10-d) (1-3-2) sequence for the third GEC installation, though the difference is not substantial (4 % smaller). The key difference lies in the influence of these maximum displacements on the region between the tube and the GEC. In the M3S2S (Fig. 12-b) configuration, the displacements were more localized near the tube tip while in the M3S2A (Fig. 10-d) sequence, they spread vertically from the tube tip up approximately 80 % of the column's length. Furthermore, on the left side of the model, the resultant displacements were smaller for M3S2S (Fig. 12-b) (1-2-3) during the installation of GEC 3 compared to M3S2A (Fig. 10-d) (1-3-2) during the installation of GEC 3, which represents the critical case. This difference may be attributed to the shielding effect in the M3S2S (Fig. 12) configuration, where the higher number of GECs provided greater protection to the area. This behavior can be beneficial for structures located near the left side of the columns, such as bridge abutment foundations, which are susceptible to lateral displacement effects, especially when constructed on soft soils (Jones et al., 2008; Schnaid et al., 2017).

3.4. Evaluation of installation on multiple GECs

The final model (M4S2S) investigated the effectiveness of installing four GECs in a row (1-2-3-4) in providing a shielding effect against hypothetical adjacent structures and mitigating the driving influence of the tube on existing columns during the installation of the last three GECs. Only the last installation (GEC 4) is shown in this analysis as the other three installations were previously studied. Only lateral displacements are evaluated in this case since vertical displacements exhibited the same behavior observed in the M3S2S model during installation of the third column. The spacing remained the same as in the three GEC models (S = 2.0 m).

Fig. 13 depicts the lateral displacements during the installation of GEC 4 in M4S2S for 25 %, 50 %, 75 % and 100 % tube driving. The lateral displacement field continued to rise as driving progressed, consistent with observations from previous models. By 25 % of tube driving (Fig. 13-a), the displacement field reached GEC 3, however, the stress increase related to the occurred displacements was insufficient to affect the column. As driving progressed, significant lateral displacements were observed on the left side of GEC 3, with values reaching approximately 0.16R starting at 50 % of driving (Fig. 13-b) and continued increasing until the end of the process (Fig. 13-d). The critical

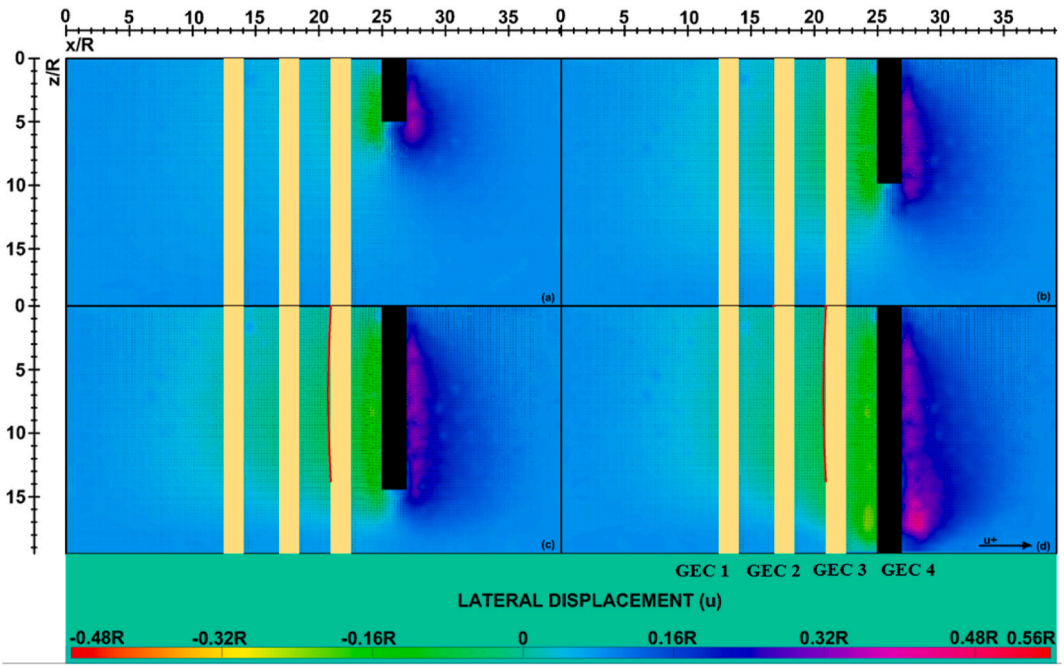

Fig. 13. Soil displacement during fourth GEC installation – M4S2S – u direction (S = 2 m): (a) 25 % of driving; (b) 50 % of driving; (c) 75 % of driving; and (d) 100 % of driving.

situation is evident from the deflection line beside GEC 3, which became apparent at 75 % of driving (Fig. 13-c) and intensified at 100 % (Fig. 13-d), highlighting the effects of cumulative displacements of the soft foundation over the column.

The analysis reveals that the maximum lateral displacements in the region between the tube and GEC 3 were approximately 0.27R, similar to those observed in the M3S2S (1-2-3 sequence) during the GEC 3 installation but these displacements have a smaller spread in the current case. The lateral displacements were localized to the left side of each column, with values reaching approximately 0.12R near GEC 3, 0.08R near GEC 2 and 0.06R near GEC 1. This indicates that soil movement during the installation process even affected the farthest columns, though these effects diminished with increasing distance. Interestingly, only GEC 3 exhibited slight deflection following tube driving while the other two columns retained their original geometries. This observation confirms the effectiveness of the four GEC configurations in shielding the left region of the model from the driving effects of the tube.

Overall, the addition of an extra GEC reduced the range of displacements on the left side of the model (opposite to GEC 4 tube driving), thereby protecting structures located in this region. Maintaining a minimum distance of 4R between the first column and any potential adjacent element is essential, as previously highlighted. The observed displacement patterns and values remained consistent when compared to the M3S2S model's third column, with only slight variations in the spatial influence area. This behavior is particularly significant for structures such as bridge abutments and foundations constructed on soft soils, which are highly vulnerable to the effects of soil lateral movement during embankment construction.

4. Conclusions

This study examined the effects of GEC installation, as quantifying displacements in the soft foundation induced by driving a tube. Reduced-scale GEC physical models on transparent soil are used to achieve the goals of the investigation. Functions were proposed to describe the displacements maximum spread curve of GEC installation effects for the case analyzed. Based on the findings of this investigation, the following conclusions were drawn:

- During tube driving, the lateral displacement field was the most impactful and presented a pattern during its propagation, the resultant displacements of which may reach adjacent GECs depending on column spacing.
- Maximum downward vertical displacements were highly localized under the tube tip, with their maximum spread decreasing as installation progressed. Conversely, although upward displacements had lower magnitudes, they extended across a larger region of the model and could potentially affect neighboring GECs or structures.
- Proposed functions had good agreement with the measured results for displacements fields and at various stages of tube penetration, although it needs further studies to be generalized for other cases.
- Increasing GEC spacing reduced the effect of soft soil movement caused by tube penetration on nearby GECs but did not eliminate it within the analyzed spacings (ranging from S = 1.0 m–2.5 m). From a spacing of 2.0 m, the displacements spread stabilized and for smaller spacing, the displacements over the neighboring GEC were significant and may potentially modify the column geometry.
- A minimum distance of 4R may be necessary between surrounding elements (e.g., other columns or structures) and the tube during installation of the first GEC to reduce the effects of lateral displacements over it.
- For the two installation sequences considered, the alternated installation showed that the confinement effect provided by the odd-numbered GECs limited the displacements caused by the third tube's driving. Conversely, when the columns were installed in a 1-2-3 sequence, the displacements (and related stresses) next to the other columns were slightly smaller. In this second case, the increased number of GECs mitigated soft soil displacements on the left side of the tube, potentially providing a shielding effect for any structures placed in that region.
- The model with four GECs sequentially installed showed a gradual reduction in displacements on the left side of the model as more columns were driven into place. This reduction can likely be attributed to the increased number of GECs creating a shielding effect, highlighting the beneficial influence of previously installed columns on the behavior of the entire system.

CRediT authorship contribution statement

H.P. Souza: Writing – original draft, Visualization, Validation, Methodology, Investigation, Data curation, Conceptualization. **G.L.S. Araújo:** Writing – review & editing, Supervision, Resources, Project administration, Funding acquisition, Formal analysis, Conceptualization. **J.G. Zornberg:** Writing – review & editing, Supervision, Funding acquisition. **F.H.M. Portelinha:** Writing – review & editing, Funding acquisition.

Declaration of competing interest

The authors declare the following financial interests/personal relationships which may be considered as potential competing interests: Gregorio Luis Silva Araujo reports financial support was provided by HUESKER Synthetic GmbH. Gregorio Luis Silva Araujo reports financial support was provided by Foundation for Research Support of the Federal District. Henrique Petisco de Souza reports financial support was provided by Coordination of Higher Education Personnel Improvement. Gregorio Luis Silva Araujo reports financial support was provided by National Council for Scientific and Technological Development. If there are other authors, they declare that they have no known competing financial interests or personal relationships that could have appeared to influence the work reported in this paper.

Acknowledgments

The authors express their acknowledgments regarding the financial support provided by Huesker Inc., CAPES/Ministry of Education of Brazil, the National Council for Scientific and Technological Development, CNPq, Brazil (Project number 404480/2021-7) and Federal District Research Foundation, Brazil (Project number 00193–00000846/2021-26)) without which this study would not be possible.

List of Symbols and Abbreviations

s_u	Undrained shear strength (kPa)
H	Soft soil layer thickness (m)
γ	Soil unit weight (kN/m^3)
ϕ'	Effective friction angle (°)
D	Diameter (mm)
T_g	Geosynthetic breaking strength (kN/m)
J_g	Stiffness at 5 % of strain (kN/m)
S	Spacing (m)
PIV	Particle Image Velocimetry
CLAHE	Contrast Limited Adaptive Histogram Equalization
W_L	Liquid limit (%)
W_P	Plastic limit (%)
IP	Plastic index (%)
k_s	Saturated hydraulic conductivity(cm/s)
e_o	Initial voids ratio
C_C	Compression index
C_R	Recompression index
MD	Machine Direction
CMD	Cross Machine Direction
C_u	Coefficient of Uniformity
C_c	Coefficient of Curvature
e_{max}	Maximum void ratio
e_{min}	Minimum void ratio
G_S	Soil specific gravity
u	Lateral displacements
u_b	Lateral displacements beside GEC
u_{max}	Maximum lateral displacements
v	Vertical displacements
v_b	Upward vertical displacements just beside GEC
v_{max}	Maximum upward vertical displacements
v^+_{max}	Maximum downward vertical displacements
R	Radius (mm)
x	Horizontal distance from the tube's side
z	Depth (m)
L	Column length (m)

Data availability

Data will be made available on request.

References

Ads, A., Iskander, M., Bless, S., 2019. Shear strength of a synthetic transparent soft clay using a miniature ball penetrometer test. Geotech. Test. J., ASTM International 43 (5), 1–22. https://doi.org/10.1520/gtj20190020.

Ads, A., Omidvar, M., Bless, S., Iskander, M., 2020. Static and dynamic analysis of torpedo anchor penetration and pullout in cohesive soils. Geo-congress 2020, American Society of Civil Engineers 283–292. https://doi.org/10.1061/9780784482803.031.

Ads, A., Islam, M.S., Iskander, M., 2021. Effect of face losses and cover-to-diameter ration on tunneling induced settlements in soft clay, using transparent soil models. Geotech.and Geol. Eng. 39 (8), 5529–5547. https://doi.org/10.1007/s10706-021-01843-7.

Al-Kazzaz, Z.A., Al-Obaydi, M.A., 2021. Effect of spacing between stone columns on the behavior of soft-soil. E3S Web of Conferences 318, 01006. https://doi.org/10.1051/e3sconf/202131801006.

Alexiew, D., Brokemper, D., Lothspeich, S., 2005. Geotextile encased columns (GEC): load capacity, geotextile selection and pre-design graphs. In: Proceedings of Geofrontiers 2005, pp. 497–510. https://doi.org/10.1061/40777(156)12. Austin, Texas, United States.

Alkhorshid, N.R., Araujo, G.L.S., Palmeira, E.M., Zornberg, J.G., 2019. Large-scale load capacity tests on a geosynthetic encased column. Geotext. Geomembranes 47 (5), 632–641. https://doi.org/10.1016/j.geotexmem.2019.103458.

Almeida, M.S.S., Hosseinpour, I., Riccio, M., Alexiew, D., 2014. Behavior of geotextile-encased granular columns supporting test embankment on soft deposit. J. Geotech. Eng. 141 (3), 1–9. https://doi.org/10.1061/(ASCE)GT.1943-5606.0001256.

Almeida, M.S.S., Riccio, M., Hosseinpour, I., Alexiew, D., 2019. Geosynthetic Encased Columns for Soft Soil Improvement. Taylor & Francis Group, London, UK. https://doi.org/10.1201/9781315177144.

Almikati, A., Pierozan, R.C., Sadek, S., Zornberg, J.G., 2023. Geotechnical characterization of laponite as transparent clay surrogate. Geotech. Test. J. 46 (3), 535–558. https://doi.org/10.1520/GTJ20220106.

Anita, A., Karthika, S., Divya, P.V., 2023. Construction and demolition waste as valuable resources for geosynthetic-encased stone columns. J. Hazard. Toxic Radioact. Waste 27 (2), 1–13. https://doi.org/10.1061/JHTRBP.HZENG-1175.

Araújo, G.L.S., Palmeira, E.M., Cunha, R.P., 2009. Behaviour of geosynthetic-encased granular columns in porous collapsible soil. Geosynth. Int. 16 (6), 433–451. https://doi.org/10.1680/gein.2009.16.6.433.

Arif, K.M., Potgieter, J., 2016. Particle image velocimetry study of displacement field in granular continua under axisymmetric conditions. 23rd International Conference on Mechatronics and Machine Vision in Practice. https://doi.org/10.1109/M2VIP.2016.7827321.

Beemer, R.D., Aubeny, C., 2012. Digital image processing of drag embedment anchors in translucent silicate gel. In: Bannister, K. (Ed.), GeoManitoba 2012. Canadian Geotechnical Society.

Beemer, R.D., Shaughnessy, E., Ewert, K.R., Boardmen, N., Biscotin, G., Aubeny, C.P., Grajales, F.J., 2016. The use of sodium pyrophosphate to improve a translucent clay simulate. Geo-chicago 2016, American Society of Civil Engineers 83–93. https://doi.org/10.1061/9780784480151.009.

Cao, Z.H., Liu, J.Y., Liu, H.l., 2011. Transparent fused silica to model natural sand. In 14th Pan-Am CGS Geotechnical Conference. International Society for Soil Mechanics and Geotechnical Engineering (ISSMGE), London, UK, paper 224.

Castro, J., 2008. Análisis teórico de la consolidación y deformación alrededor de columnas de grava. Tesis Doctorales en Red. ISBN: 978-84-691-5966-8.

Castro, J., Karstunen, M., 2010. Numerical simulations of stone column installation. Can. Geotech. J. 47, 1127–1138. https://doi.org/10.1139/T10-019.

Cengiz, C., Guler, E., 2020. Sample preparation method for large scale shear testing of soft-clay and granular column composites. MethodsX 7, 1–12. https://doi.org/10.1016/j.mex.2020.100939.

Chen, J.F., Gu, Z.A., Rajesh, S., Yu, S.B., 2021. Pullout behavior of triaxial geogrid embeddedin a transparent soil. Int. J. Geomech. 21 (3), 04021003. https://doi.org/10.1061/(ASCE)GM.1943-5622.0001936.

Chen, J.F., Zhang, X., Yoo, C., Gu, Z.A., 2022. Effect of basal reinforcement on performance of floating geosynthetic encased stone column-supported embankment. Geotext. Geomembranes 50 (4), 566–580. https://doi.org/10.1016/j.geotexmem.2022.01.006.

Chini, C.M., Wallace, J.F., Rutherford, J.F., Peschel, J.M., 2015. Shearing failure visualization via particle tracking in soft clay using a transparent soil. Geotech. Test. J. 38 (5), 1–17. https://doi.org/10.1520/GTJ20140210.

Engin, H.K., Brinkgreve, R.B.J., van Tol, A.F., 2015. Simplified numerical modelling of pile penetration – the press-replace technique. Int. J. Numer. Methods Eng. 39 (15), 1713–1734. https://doi.org/10.1002/nag.2376.

Ergin, F.G., 2021. An automatic static masking technique using particle image velocimetry image ensembles. Exp. Therm. Fluid Sci. 128, 110431–110440. https://doi.org/10.1016/j.expthermflusci.2021.110431.

Ezzein, F.M., Bathurst, R.J., 2014. A new approach to evaluate soil-geosynthetic interaction using a novel pullout test apparatus and transparent granular soil. Geotext. Geomemb. 42 (3), 246–255. https://doi.org/10.1016/j.geotexmem.2014.04.003.

Fakhariam, K., Khanmohammadi, M., 2022. Effect of OCR and pile diameter on load movement response of piles embedded in clay over time. (ASCE). Int. J. GeoMech. 22 (7), 04022091. https://doi.org/10.1061/(ASCE)GM.1943-5622.0002419.

Fattah, M.Y., Zabar, B.S., Hassan, H.A., 2016. Experimental analysis of embankment on ordinary and encased stone columns. Int. J. GeoMech. 16 (4), 04015102. https://doi.org/10.1061/(ASCE)GM.1943-5622.0000579.

FHWA (Federal Highway Administration), 1980. Highway sub-drainage design manual. FHWA-TS-80-224, 1:1-162.

Geramian, A., Castro, J., Ghazavi, M., Miranda, M., 2022. Installation of groups of stone columns in clay: 3D coupled eulerian lagranrian analyses. Comput. Geotech. 151, 1–10. https://doi.org/10.1016/j.compgeo.2022.104931.

Hanna, A., Khalifa, M., Rahman, M.A., 2019. Experimental investigation on stone columns in cohesive soil. GeoMEast, 2018. https://doi.org/10.1007/978-3-030-01917-4_14.

Helm, J., Suleiman, M., 2012. Measuring soil-structure interaction on laterally loaded piles with digital image correlation. Proc. IUTAM 4, 66–72. https://doi.org/10.1016/j.piutam.2012.05.008.

Hong, Y., Wu, C., Yu, Y., 2016. Model tests on geotextile-encased granular columns under 1-g and undrained conditions. Geotext. Geomembranes 44 (1), 13–27. https://doi.org/10.1016/j.geotexmem.2015.06.006.

Hosseinpour, I., Almeida, M.S.S., Riccio, M., 2015. Full-scale load test and finite-element analysis of soft ground improved by geotextile-encased granular columns. Geosynth. Int. 22 (6), 428–438. https://doi.org/10.1680/jgein.15.00023.

Hosseinpour, I., Almeida, M.S.S., Riccio, M., 2016. Ground improvement of soft soil by geotextile-encased columns. Ground Improv. 169 (GI4), 297–305. https://doi.org/10.1680/jgrim.16.00009.

Iskander, M., 2010. Modelling with Transparent Soils: Visualizing Soil Structure Interaction and Multi Phase Flow, Non-intrusively. Springer. https://doi.org/10.1007/978-3-642-02501-3.

Jones, C.A., Stewart, D.I., Danilewicz, C.J., 2008. Bridge distress caused by approach embankment settlement. Geotech. Eng. 161 (2), 63–74. https://doi.org/10.1680/geng.2008.161.2.63.

Kelesoglu, M.K., Durmus, C., 2022. Numerical plane-strain modelling of stone columns: Installation process, single and group column behaviour. J. Civ. Eng. 26 (8), 3402–3415. https://doi.org/10.1007/s12205-022-1671-3.

Kempfert, H.G., Gebreselassie, B., 2006. Excavations and Foundations in Soft Soils, vol. 591p. Springer, New York. https://doi.org/10.1007/3-540-32895-5.

Khatami, H., Deng, A., Jaksa, M., 2019. An experimental study of the active arching effect in soil using the digital image correlation technique. Comput. Geotech., Elsevier B 108, 183–196. https://doi.org/10.1016/j.compgeo.2018.12.023.

Kim, I., Kim, G., Lee, J., 2022. Centrifuge investigation of groundwater-induced footing settlement in sand considering rising and falling GWL phases. J. Geotech. Geoenviron. Eng. 148 (11), 1–12. https://doi.org/10.1061/(ASCE)GT.1943-5606.0002920.

Kirsch, F., 2004. Experimentelle und numerische Untersuchungen zum Tragverhalten von Rüttelstopfsäulengruppen". Disertation. TU Braunschweig.

Li, H., Tang, C., Cheng, Q., Li, S., Gong, X., Shi, B., 2019. Tensile strength of clayey soil and the strain analysis based on image processing techniques. Eng. Geol. 253, 137–148. https://doi.org/10.1016/j.enggeo.2019.03.017.

Liu, C., Tang, X., Wei, H., Wang, P., Zhao, H., 2020. Model Tests of Jacked-Pile Penetration into Sand Using Transparent Soil and Incremental Particle Image Velocimetry. KSCE J. Civ. Eng. 24 (4), 1228–11445. https://doi.org/10.1007/s12205-020-1643-4.

Ma, S., Wei, H., Duan, Z., Liu, Y., Huang, Z., He, B., Zhou, Z., 2023. Transparent soil model test and numerical study on the effect of adjacent spring on the stability of tunnel face in composite strata. Nat. Haz. 118, 495–524. https://doi.org/10.1007/s11069-023-06015-9.

Massarsch, K.R., Wersäll, C., 2013. Cumulative soil displacement due to pile driving in soft clay. In: Stuedlein, Armin W., Christopher, Barry R. (Eds.), Sound Geotechnical Research to Practice, Geotechnical Special Publication (GSP 230) Honoring Robert D. Holtz, pp. 463–480. https://doi.org/10.1061/9780784412770.031. Ph.D., P.E., ASCE.

Nagula, S.S., Nguyen, D.M., Grabe, J., 2018. Numerical modelling and validation of geosynthetic encased columns in soft soils with installation effect. Geotext. Geomembranes 46 (6), 790–800. https://doi.org/10.1016/j.geotexmem.2018.07.011.

Orekanti, E.R., Dommaraju, G.V., 2019. Load-settlement response of geotextile encased laterally reinforced granular piles in expansive soil under compression. Int. J. of Geosynth. Ground Eng. 5 (3), 1–8. https://doi.org/10.1007/s40891-019-0168-8.

Ouyang, F., Wu, Z., Wang, Y., Wang, Z., Cao, J., Wang, K., Zhang, J., 2024. Field tests on partially geotextile encased stone column-supported embankment over silty clay. Geotext. Geomemb. 52, 95–109. https://doi.org/10.1016/j.geotexmem.2023.09.005.

Peng, X., Zornberg, J.G., 2019. Evaluation of soil-geogrid interaction using transparent soil with laser illumination. Geosynth. Int. 26 (2), 206–221. https://doi.org/10.1680/jgein.19.00004.

Pierozan, R.C., Almikati, A., Araújo, G.L.S., Zornberg, J.G., 2021. Optical and physical properties of laponite for use as clay surrogate in geotechnical models. Geotech. Test. J. 45 (1), 79–100. https://doi.org/10.1520/GTJ20210100.

Ren, M., Jiang, T., Liu, C., Zhang, J., Wang, L., 2022. Deformation characteristics of sandy soil around a plate anchor under lateral loading. Geofluids 2022, 1–16. https://doi.org/10.1155/2022/1117143.

Ren, J., Zhang, S., Ishikawa, T., Li, S., Wang, C., 2023. The frost heave characteristics of a coarse-grained volcanic soil quantified by particle image velocimetry. Geoderma 430, 116352–116372. https://doi.org/10.1016/j.geoderma.2023.116352.

Salehzadeh, H., Nuri, H., Rafsanjani, A.A.H., 2022. Failure mechanism of helical anchors in sand by centrifuge modeling and PIV. Int. J. GeoMech. 22 (8), 1–20. https://doi.org/10.1061/(ASCE)GM.1943-5622.0002422.

Schnaid, F., Winter, D., Silva, A.E.F., Alexiew, D., Küster, 2017. Geotextile encased columns (GEC) used as pressure-relief system. Instrumented bridge abutment case study on soft soil. Geotext. Geomembranes 45 (3), 227–236. https://doi.org/10.1016/j.geotexmem.2017.02.003.

Sharifi, S., Abrishami, S., Dias, D., Dastpak, P., 2022. Behavior of axially and eccentrically loaded trapezoidal shell footings resting on a granular assembly. Int. J. GeoMech. 22 (8), 1–12. https://doi.org/10.1061/(ASCE)GM.1943-5622.0002442.

Shehata, H.F., Sorour, T.M., Fayed, A.L., 2018. Effect of stone column installation on soft clay behavior. Int. J. Geotech. Eng. 15 (5), 530–542. https://doi.org/10.1080/19386362.2018.1478245.

Stanier, S.A., Blaber, J., Take, W.A., White, D.J., 2016. Improved image-based deformation measurement for geotechnical applications. Can. Geotech. J. 53 (5), 727–739. https://doi.org/10.1139/cgj-2015-025.

Thielicke, W., Stamhuis, E.J., 2014. PIVlab – towards user-friendly, affordable and accurate digital particle image velocimetry in MATLAB. J. Open Res. Software 2 (1), e30. https://doi.org/10.5334/jors.bl.

Wallace, J.F., Rutherford, C.J., 2015. Geotechnical properties of LAPONITE RD®. Geotech. Test. J. 38 (5), 574–587. https://doi.org/10.1520/GTJ20140211.

Wang, K., Liu, M., Cao, J., Niu, J., Zhuang, Y., 2023. Bearing characteristics of composite foundation reinforced by geosynthetic-encased stone column: field tests and numerical analyses. Sustainability 15 (5965), 1–15. https://doi.org/10.3390/su15075965.

Watts, K.S., Johnson, D., Wood, L.A., Saadi, A., 2000. Instrumental trial of vibro ground treatment supporting strip foundations in a variable fill. Geotechnique 50 (6), 699–709. https://doi.org/10.1680/geot.2000.50.6.699.

Wu, C.S., Hong, Y.S., 2014. A simplified approach for evaluating the bearing performance of encased granular columns. Geotext. Geomembranes 42 (4), 339–347. https://doi.org/10.1016/j.geotexmem.2014.05.006.

Xu, Z., Zhang, L., Zhou, S., 2021. Influence of encasement length and geosynthetic stiffness on the performance of stone column: 3D DEM-FDM coupled numerical investigation. Comput. Geotech. 132, 1–15. https://doi.org/10.1016/j.compgeo.2020.103993.

Yang, Q., Shao, J., Xu, Z., Miao, Y., 2022. Experimental investigation of the impact of necking position on pile capacity assisted with transparent soil technology. Adv. Civ. Eng. 2022 (1), 1–10. doi:10.1155/2022/9965974.

Yuan, B., Sun, M., Xiong, L., Luo, Q., Pradhan, S.P., Li, H., 2020. Investigation of 3D deformation of transparent soil around a laterally loaded pile based on a hydraulic gradient model test. J. Build. Eng. 28, 101024. https://doi.org/10.1016/j.jobe.2019.101024.

Zhang, Y., Hu, M., Ye, T., Chen, Y., Zhou, Y., 2019. An experimental study on the rheological properties of laponite RD as a transparent soil. Geotech. Test. J. 43 (3), 1–16. https://doi.org/10.1520/GTJ20180348.

Zhou, P., Li, J., Li, L., Xie, F., 2021. Analysis of the existing pile response induced by adjacent pile driving in undrained clay. Comput. Geotech. 138, 104319–104347. https://doi.org/10.1016/j.compgeo.2021.104319.